

# Surface photometry of BCGs and intracluster stars in $\Lambda$ CDM

A. P. Cooper<sup>1\*</sup>, L. Gao<sup>1,2</sup>, Q. Guo<sup>1</sup>, C.S. Frenk<sup>2</sup>, A. Jenkins<sup>2</sup>, V. Springel<sup>3,4</sup>, S.D.M. White<sup>5</sup>

<sup>1</sup>National Astronomical Observatories, Chinese Academy of Sciences, 20A Datun Road, Chaoyang, Beijing 100012, China

<sup>2</sup>Institute for Computational Cosmology, Department of Physics, University of Durham, South Road, Durham, DH1 3LE, UK

<sup>3</sup>Heidelberg Institute for Theoretical Studies, Schloss-Wolfsbrunnengasse 35, D-69118 Heidelberg, Germany

<sup>4</sup>Zentrum für Astronomie der Universität Heidelberg, ARI, Mönchhofstr. 12-14, D-69120 Heidelberg, Germany

<sup>5</sup>Max-Planck-Institut für Astrophysik, Karl-Schwarzschild-Str. 1, D-85748, Garching, Germany

Accepted xxxx. Received xxxx; in original form xxxx

## ABSTRACT

We simulate the phase-space distribution of stellar mass in 9 massive  $\Lambda$ CDM galaxy clusters by applying the semi-analytic particle tagging method of Cooper et al. to the Phoenix suite of high-resolution N-body simulations ( $M_{200} \approx 7.5\text{--}33 \times 10^{14} M_{\odot}$ ). The resulting surface brightness (SB) profiles of brightest cluster galaxies (BCGs) match well to observations. On average, stars formed in galaxies accreted by the BCG account for  $\gtrsim 90$  per cent of its total mass (the remainder is formed in situ). In circular BCG-centred apertures, the superposition of multiple debris clouds (each  $\gtrsim 10$  per cent of the total BCG mass) from different progenitors can result in an extensive outer diffuse component, qualitatively similar to a ‘cD envelope’. These clouds typically originate from tidal stripping at  $z \lesssim 1$  and comprise both streams and the extended envelopes of other massive galaxies in the cluster. The faint regions of the BCG contribute a significant part of the total cluster stellar mass budget: in the central  $1 \text{ Mpc}^2$  of a  $z \sim 0.15$  cluster imaged at SDSS-like resolution, our fiducial model predicts 80–95 per cent of stellar mass below a SB of  $\mu_V \sim 26.5 \text{ mag arcsec}^{-2}$  is associated with accreted stars in the envelope of the BCG. The ratio of BCG stellar mass to total cluster stellar mass is  $\sim 30$  per cent.

**Key words:** galaxies: clusters: general; galaxies: elliptical and lenticular, cD; galaxies: photometry; galaxies: haloes; galaxies: structure; methods: numerical

## 1 INTRODUCTION

Observations of diffuse intracluster light (ICL) have shown that many stars in galaxy groups and clusters are ‘outside’ the galaxies themselves (Zwicky 1951). The stars responsible for ICL are thought to have been tidally stripped from cluster galaxies (Gallagher & Ostriker 1972; Ostriker & Tremaine 1975; Richstone 1975; White 1976; Hausman & Ostriker 1978; Merritt 1984). On this basis, N-body simulations have shown that the gross structural and dynamical characteristics of ICL and the central (‘brightest’) galaxies of clusters (BCGs) can be reproduced within the context of the  $\Lambda$ CDM cosmogony (Moore et al. 1996; Dubinski 1998; Napolitano et al. 2003; Murante et al. 2004; Willman et al. 2004; Diemand et al. 2005; Sommer-Larsen et al. 2005; Rudick et al. 2006; Murante et al. 2007; Ruzsowski & Springel 2009; Dolag et al. 2010; Puchwein et al. 2010; Oser et al. 2010; Laporte et al. 2013).

The surface brightness profile is one of the most easily studied observables of BCGs. Idealized N-body simulations have been used to predict how these profiles evolve through successive generations of mergers between cluster galaxies (e.g. Naab et al. 2009; Hilz et al.

2012, 2013; Laporte et al. 2012, 2013). However, these simulations do not usually include a realistic treatment of in situ star formation in galaxies, and this limits their ability to make quantitative predictions for real BCGs. Specifically, gas dissipation strongly biases the phase space distribution of stars relative to that of dark matter, such that stars generally trace the deepest parts of dark matter potential wells (e.g. Gao et al. 2004; Diemand et al. 2005). In detail this bias depends on when, where and in what quantity stars form within the evolving hierarchy of dark matter structures (Frenk et al. 1985). Only some of the more recent cluster N-body simulations have addressed the strong observational constraints on these factors (e.g. Laporte et al. 2013).

The baryonic processes regulating galaxy formation – gas cooling, star formation, ‘feedback’ from supernovae and active galactic nuclei (AGN) – can be included self-consistently in hydrodynamic simulations, at least in principle. In practice, most of these processes act on scales below the resolution of current hydrodynamic solvers and thus have to be implemented with ad hoc semi-analytic recipes. Long run times make it hard to compare different implementations and test numerical convergence, leading to large variations between the results of different groups (e.g. Scannapieco et al. 2012) and uncertain agreement with the statistics of

\* E-mail: acooper@nao.cas.cn

the present-day galaxy population. Although these problems are now arguably under control for simulations of individual galaxies, they remain relevant for simulations of galaxy formation in clusters. For example, recent hydrodynamic simulations have claimed that AGN feedback is required to produce realistic BCG masses and ICL fractions (Puchwein et al. 2010; Martizzi et al. 2012). Cluster simulations with supernova feedback alone result in BCG stellar masses much higher than those observed (e.g. Oser et al. 2010; Rudick et al. 2011).

Semi-analytic models have had more success in making quantitative predictions that agree well with the statistical properties of large surveys, including observed scaling relations for BCGs (Aragon-Salamanca et al. 1998; De Lucia & Blaizot 2007; Conroy et al. 2007; Purcell et al. 2007; Bower et al. 2008; Guo et al. 2011). However, most semi-analytic models represent galactic structure with 1-dimensional axisymmetric ‘disk’ and ‘bulge’ density profiles of predetermined form<sup>1</sup>. As galaxies merge, changes in the mass and size of their structural components are approximated with simple energy conservation laws based on the virial theorem and parameterized to match idealized N-body simulations (Cole et al. 2000; Guo et al. 2011). Average scaling relations can be studied with these approximations. However, predictions for observations of massive merger remnants, including BCG and ICL surface brightness profiles, need a more detailed and self-consistent description of how the stars from each individual progenitor evolve in phase space.

Here we bridge this particular gap between  $N$ -body and semi-analytic models by using the N-body particle-tagging technique of Cooper et al. (2010, 2013, hereafter C13) in combination with the ab initio  $\Lambda$ CDM semi-analytic model of Guo et al. (2011, hereafter G11). This technique allows us to make quantitative predictions for the 6-dimensional phase space distribution of stars that form in semi-analytic galaxies, which can be compared directly to observations. Using the G11 model ensures that the star formation histories in our simulations are compatible with the statistics of the present-day galaxy population. Our aim is to make  $\Lambda$ CDM-based predictions for the stellar mass surface density profiles of accreted stars in cluster BCGs and their associated ICL, and to help interpret recent observational work on the fraction of stellar mass in clusters that belongs to these components.

We proceed as follows. Our simulations are described in section 2. Images of the simulated clusters are shown in section 3. Section 4 describes the surface density profiles of BCGs and compares them to observations. Section 5 analyzes the shape of these profiles in terms of the contribution of individual accreted substructures. Section 6 discusses the relative fractions of stars in different stellar components. We summarise and conclude in section 7. Appendix A discusses important numerical issues.

## 2 METHOD

### 2.1 Definitions of BCG and ICL

Explicit definitions for terms like BCG and ICL are essential, because galaxies do not have clear boundaries (Zwicky 1951). We call the galaxy at the centre of the potential well of the cluster ‘the

BCG’ even though that central galaxy may not be the brightest in all filters or apertures. We *do not* separate intracluster stars from BCG stars<sup>2</sup>. Instead, we treat the BCG as a single entity consisting of all stars which are not bound to any subhaloes in the cluster (as identified by the SUBFIND algorithm; Springel et al. 2001). As well as stars bound only to the main cluster halo, this includes a small fraction of unbound stars within  $R_{200}$  ( $\sim 1$  per cent of the BCG stellar mass). As we demonstrate below, this definition of the BCG includes many stars in low surface brightness regions far from the centre of the cluster.

Among BCG stars, we distinguish *accreted stars*, which have been stripped from galaxies other than the BCG, from *in situ* stars, which formed directly from the cluster cooling flow. In a simulation, the distinction between in situ and accreted stars is technically simple and almost unambiguous<sup>3</sup>. This contrasts with more sophisticated dynamical definitions of the ICL, which separate stars bound to the ‘cluster potential’ from those bound to (the stellar component of) the BCG (Dolag et al. 2010; Puchwein et al. 2010; Rudick et al. 2011). We will argue that the accreted/in situ separation is physically meaningful because ICL phenomena in massive clusters are driven by trends in the accreted component with  $M_{200}$ .

Given these definitions, we only use the term ICL in a very loose sense, to refer to the observational phenomenon of light from low surface brightness regions in galaxy clusters. Whenever we compare to observations, we do not attempt any BCG/ICL or in situ/accreted separation (following, for example, Lin & Mohr 2004).

### 2.2 Phoenix and Millennium II

Phoenix is a suite of 9 high resolution dark matter-only N-body simulations of very massive  $\Lambda$ CDM galaxy clusters, resimulated using a ‘zoom’ technique with initial conditions drawn from the Millennium Simulation (Gao et al. 2012). The particle mass ranges from  $m_p = 6.1 \times 10^6 M_\odot$  (Ph-E) to  $2.5 \times 10^7 M_\odot$  (Ph-I), such that there are approximately 130 million particles within  $r_{200}$  in each cluster halo at  $z = 0$ . Bound dark matter haloes and subhaloes were identified with the SUBFIND algorithm. Relevant properties of the cluster halo in each simulation are summarized in Table 1. The application of the G11 semi-analytic galaxy formation model to Phoenix is described separately by Q. Guo et al. (in preparation). In certain figures we show a sample of less massive clusters from C13 based on the Millennium II simulation (Boylan-Kolchin et al. 2010), which has comparable resolution ( $m_p = 9.4 \times 10^6 M_\odot$ ).

Our simulations use a cosmology compatible with WMAP 1 ( $\Omega_m = 0.25$ ,  $\Omega_\Lambda = 0.75$ ,  $n_s = 1$ ,  $\sigma_8 = 0.9$ ) and we assume a Hubble parameter  $h = 0.73$  throughout (we convert data from other authors accordingly). More recent limits from the cosmic microwave background amount to a rescaling in the mass, size and abundance of our clusters, but do not alter the trends in our galaxy formation model significantly, beyond their effect on star formation histories through dark matter halo collapse times (Guo et al. 2013). Such changes are likely to be smaller than the current observational uncertainties in BCG masses and sizes (e.g. Bernardi et al. 2013).

<sup>1</sup> Some have recently introduced ‘intracluster light’ components that grow in mass through tidal stripping, without specifying how those stars are distributed (Monaco et al. 2006; Henriques & Thomas 2010; Guo et al. 2011; Contini et al. 2014).

<sup>2</sup> By considering the ICL to be part of the BCG, we effectively ensure that the central galaxy is the most luminous.

<sup>3</sup> The main ambiguity is that in identifying a unique ‘main branch’ of the halo merger tree, particularly at high redshift when equal mass mergers are common.

**Table 1.** Properties of the Phoenix cluster simulations (Gao et al. 2012) and new results for their BCGs discussed in this paper. The table is ordered by  $M_{200}$ . From left to right columns show: (1) the simulation label; (2)  $M_{200}$  [ $10^{14} M_{\odot}$ ]; (3)  $R_{200}$  [Mpc]; (4)  $M_{500}$  [ $10^{14} M_{\odot}$ ]; (5) redshift of half mass assembly for the cluster dark matter,  $z_h$ ; (6) the total stellar mass *including stars associated with galaxies below the resolution limit*,  $M_{\text{BCG}}^{\text{all}}$  [ $10^{12} M_{\odot}$ ]; (7) the fraction of this mass formed in situ; (8) the fraction accreted; (9) the fraction of all stars associated with sub-resolution galaxies (see text); (10) the fraction associated with streams from surviving galaxies with resolved haloes; (11) the total stellar mass bound to resolved dark matter subhalos of the cluster [ $10^{12} M_{\odot}$ ] (this does not include stars associated with sub-resolution haloes); (12) the number of significant progenitors of the accreted component of the BCG [see section 5.1]; (13) the number of progenitors accounting for 50 per cent of the accreted mass of the BCG; (14) the number accounting for 90 per cent; (15) the effective radius of the BCG (mean of 3 orthogonal projections) including sub-resolution galaxy stars [kpc]; (16) the effective radius when sub-resolution galaxy stars are excluded [kpc].

Name	$M_{200}$	$R_{200}$	$M_{500}$	$z_h$	$M_{\text{BCG}}^{\text{all}}$	% <sub>ins</sub>	% <sub>acc</sub>	% <sub>subres</sub>	% <sub>streams</sub>	$M_{\text{sat}}^{\text{min}}$	$N_{\text{prog}}$	$N_{50}$	$N_{90}$	$R_{50}^{\text{all}}$	$R_{50}^{\text{excl}}$
[1]	[2]	[3]	[4]	[5]	[6]	[7]	[8]	[9]	[10]	[11]	[12]	[13]	[14]	[15]	[16]
C	7.527	1.899	5.884	0.76	5.40	8.3	91.7	18.1	21.8	7.09	9.76	6	61	103	82.4
E	8.176	1.912	6.414	0.91	4.81	12.0	88.0	24.1	21.6	6.59	15.9	7	105	125	86.0
D	8.481	1.899	6.239	0.46	4.22	14.3	85.7	25.9	27.6	9.07	17.8	8	101	39.0	89.8
A	9.000	1.937	7.278	1.17	5.68	8.4	91.6	28.4	25.3	6.60	25.1	22	274	185	155
F	10.93	2.067	8.324	1.10	5.27	13.7	86.3	13.2	25.4	9.69	25.2	11	234	132	117
B	11.31	2.090	8.387	0.46	6.44	6.5	93.5	29.8	30.0	9.65	7.80	5	74	178	181
H	15.55	2.310	11.88	0.21	9.31	19.5	80.5	28.1	26.5	16.0	13.6	9	190	186	100
G	15.75	2.334	10.82	0.18	5.14	9.9	90.1	33.2	30.5	16.3	17.0	7	190	296	171
I	33.03	2.933	25.50	0.56	20.7	5.48	94.5	30.6	35.2	30.0	43.1	27	657	314	284

### 2.3 Particle Tagging

Our particle tagging technique is described in Cooper et al. (2010) and its application to massive galaxies in C13, to which we refer the reader for further details. The fundamental idea is to use a weighted subset of dark matter particles in a cosmological  $N$ -body simulation to approximate the phase space evolution of stellar populations. Our method improves on similar techniques that have been applied to BCG models in the past (White 1980; Napolitano et al. 2003; Gao et al. 2004; Diemand et al. 2005; Laporte et al. 2012, 2013). Our application is novel in several respects: the tagging is coupled directly to the star formation predictions of the semi-analytic model, which in turn is constrained to reproduce the  $z = 0$  stellar mass function; it tags in situ stars at the time of their formation, rather than composite galaxies at the time of their accretion; and the tagging method is constrained to reproduce the  $z = 0$  mass–size relation for galaxies dominated by in situ stars, as described below.

We first process the merger trees of the simulation with the G11 model and identify each ‘single age’ stellar population (SSP) that forms between two successive snapshots (a galaxy at any time is the sum of many SSPs). For each SSP, we identify all the dark matter particles in the corresponding halo at the later of the two bracketing snapshots, rank them by their binding energy and select a fixed fraction,  $f_{\text{mb}}$ , in rank order starting from the most bound particle. This approximates the end result of the dissipative collapse of gas prior to star formation, namely that newly formed stars are more tightly bound than the bulk of the dark matter in the halo (White & Rees 1978). Each of these tightly bound particles is tagged with an equal fraction of the stellar mass in the SSP. A single dark matter particle can be tagged with stars from several SSPs that form at different snapshots.

In an NFW halo, our constant- $f_{\text{mb}}$  tagging method selects a subregion of the overall dark matter distribution function that corresponds to a truncated exponential density profile when integrated over velocity space and one dimension of configuration space (i.e. the projection of the galaxy along the line of sight; see C13). In a smoothly growing halo such profiles transform into pure exponentials over time as particles diffuse above the initial cut-off energy corresponding to  $f_{\text{mb}}$ . The exponential scale lengths of these profiles scale systematically (albeit weakly) with the value of  $f_{\text{mb}}$ . As discussed in C13, for a given  $N$ -body halo of known mass and

concentration, the scale length obtained from particle tagging can be predicted using a spherically symmetric and isotropic approximation to the NFW distribution function (e.g. Widrow 2000).

By assuming a constant universal value of  $f_{\text{mb}}$  and that all stars in a given  $z = 0$  halo form at a single time, it is straightforward to apply this approximation to the population of dark matter haloes in a cosmological simulation and thereby compute a relation between  $M_{\star}$  and half-mass radius ( $R_{50}$ ) for galaxies of  $M_{\star} \lesssim 10^{10} M_{\odot}$  (i.e. the regime where  $M_{\star}$  is dominated by in situ star formation rather than accretion; Guo & White 2008). The size-mass relation inferred in this way will simply reflect the statistics of the halo mass–concentration relation and the  $M_{\star}$ – $M_{200}$  relation, but is nevertheless a good approximation to the results of full particle tagging based on semi-analytic star formation histories. Specifically, once the  $M_{\star}$ – $M_{200}$  relation is fixed, the normalization of  $R_{50}(M_{\star})$  in this approximation is determined by  $f_{\text{mb}}$ . By comparing such predictions to observations, C13 found a range of acceptable values  $1 \lesssim f_{\text{mb}} \lesssim 3$  per cent. We use only  $f_{\text{mb}} = 1$  per cent here (see appendix A).

As discussed in C13, our method may underestimate the central densities and internal binding energies of late-type galaxies (and thus overestimate their sizes) because we do not explicitly model the dynamics of the dissipative collapse of cold gas and we neglect the adiabatic contraction of dark matter due to baryons (e.g. Gnedin et al. 2004). However, recent work predicts only mild contraction for star formation efficiencies compatible with observations (Dutton et al. 2007; Abadi et al. 2010, Schaller et al. in prep.) and also a counteracting expansion due to feedback (Navarro et al. 1996; Pontzen & Governato 2012). Moreover, this paper is focused on early-type galaxies, which result from mergers occurring at  $z < 1$ , after the majority of stars have formed in their progenitors (in our model, in situ star formation triggered by low redshift mergers only accounts for a small fraction of the mass in present-day BCGs). Violent relaxation in low mass ratio mergers and dynamical friction acting on infalling substructures can reduce the central density cusps created by any dissipative contraction at high redshift and can simultaneously increase the central dark matter mass fraction (El-Zant et al. 2001; Gao et al. 2004; Ruszkowski & Springel 2009; Hilz et al. 2012; Laporte et al. 2012; Remus et al. 2013). Strong lensing observations of the total mass profiles of massive early-type galaxies imply very little net modification of the dark

matter in the inner regions despite the central concentration of stars (Newman et al. 2013b,a; Dutton & Treu 2014). On the other hand, hydrodynamical simulations have shown that baryonic effects can alter the dark matter distribution even in the outer parts of massive haloes (van Daalen et al. 2011).

### 3 IMAGES

Fig. 1 shows 1 Mpc  $\times$  1 Mpc stellar mass surface density images of the Phoenix clusters, including both stars bound to the cluster potential (which we identify with the BCG) and stars bound to subhaloes (which we identify with other cluster members). The ‘diffuse’ light around the BCG is very anisotropic, extends to the edge of these images and contains several relatively bright and coherent streams in most of our clusters (e.g. at approximately  $(X, Y) = (600, -250)$  in Ph-C). Extensive diffuse light and a handful of bright streams have been observed in nearby clusters (Conselice & Gallagher 1999; Feldmeier et al. 2004), particularly Virgo (Mihos et al. 2005; Rudick et al. 2010; Janowiecki et al. 2010); Centaurus, with a  $\sim 170$  kpc  $\times$  3 kpc stream of  $\mu_R \sim 26.1$  mag arcsec $^{-2}$  (Calcáneo-Roldán et al. 2000); and Coma (e.g. Melnick et al. 1977; Thuan & Kormendy 1977; Trentham & Mobasher 1998; Adami et al. 2005) which has a broad stream of length  $\sim 130$  kpc, width 15–30 kpc,  $\mu_R \sim 25.7$  mag arcsec $^{-2}$  and no obvious progenitor (Gregg & West 1998).

Fig. 2 shows the central  $300 \times 300$  kpc region of Ph-A in more detail. Panels 0, 1 and 2 show how the appearance of the BCG changes with projection along orthogonal axes of the simulation box – all BCGs are significantly elongated along one axis, although this has little effect on any of the properties described in this paper. Panel 3 shows only stars that have been accreted by the BCG and which are not associated with any surviving satellite in the semi-analytic model; panel 4 shows stars formed in situ in the main branch of the BCG’s merger tree. These components show similar alignment and elongation<sup>4</sup>, both of which can be attributed to the one or two most recent ‘major’ merger events (see e.g. Cooper et al. 2011 for a high resolution visualization of this effect in a less massive elliptical galaxy).

Panel 5 of Fig. 2 shows stars associated with surviving well-resolved galaxies, including those that are still bound (visible as obvious concentrations) and those that have been stripped into the accreted component of the BCG. Many of the bright galaxies around the BCG contribute a substantial mass of tidal debris, to the extent that the overall distribution looks rather uniform because individual tidal streams have low contrast against the bulk of diffuse material.

#### 3.1 Stars associated with sub-resolution haloes and other numerical issues

In the G11 model, semi-analytic galaxies can survive even after tidal stripping reduces the mass of their associated dark matter subhalo below the 20-particle resolution limit of SUBFIND. G11 assume that no stars are stripped from these galaxies associated with unresolved haloes (called orphans or ‘type 2’ galaxies elsewhere) until they merge or are (instantaneously) destroyed by tides. In this paper, we choose to assign all of the stars associated with these galaxies to the accreted component of the BCG. In other words, we

assume that subhaloes will have lost essentially all of their stellar mass by the time they are stripped below a total mass of 20 particles ( $\sim 2 \times 10^8 M_\odot$ ).

A detailed discussion of this variation to the G11 model is given in appendix A, where we argue it is justified by the neglect of stellar stripping in G11. To summarise, in the case of a Milky Way-like halo having  $M_{200} \sim 10^{12} M_\odot$  at infall, the 20 particle resolution limit corresponds to a remnant halo mass fraction of only  $\sim 0.02$  per cent; it seems implausible that 100 per cent of the stars in such a halo would remain bound after such dramatic dark matter mass loss, as the G11 model assumes. However, for dwarf galaxy haloes with maximum pre-infall mass close to  $10^8 M_\odot$ , the corresponding fractional mass loss required to fall below the resolution limit is much smaller and hence the assumption that *all* stars bound to unresolved halo remnants have been stripped is less accurate. The net contribution of stars from these less massive haloes could, in principle, make a significant difference to our conclusions. In appendix A we show alternative results for the case where all stars from sub-resolution haloes are excluded from the definition of the BCG (and hence treated as stars in surviving galaxies).

Panel 5 of Fig. 2 shows the subset of stars in question, those that belong to the accreted component of the BCG according to the  $N$ -body part of our model but are associated with surviving sub-resolution haloes in the semi analytic part. Clearly (almost by definition) the vast majority of these are not concentrated in galaxy-like clumps. Rather, they are spread out all over the halo, much like the stars stripped from well resolved subhaloes (panel 4). They are more centrally concentrated in the cluster, consistent with the defunct subhaloes either having radial orbits (those lost due to rapid disruption) or having orbited for a long time in the centre of the cluster (those lost due to prolonged stripping).

Panel 7 of Fig. 2 shows the same halo simulated at lower resolution and panel 8 the result of choosing  $f_{\text{mb}} = 5$  per cent at our standard resolution – neither of these makes a substantial difference to the overall appearance of the BCG, although there are subtle changes to the density distribution. Appendix A also addresses these numerical issues in more detail.

## 4 SURFACE DENSITY/BRIGHTNESS PROFILES

### 4.1 Phoenix clusters

Fig. 3 shows  $\Sigma_*(R)$ , the azimuthally averaged<sup>5</sup> stellar mass surface density of stars associated with the BCG in each Phoenix cluster at  $z = 0$ , according to the definition in Section 1, i.e. all stars tagged to DM particles bound to the potential well of the cluster’s dark matter halo but not to any of its subhaloes.

Although our clusters span a factor of 4 in  $M_{200}$ , their central galaxies have remarkably similar  $\Sigma_*(R)$  profiles. The cluster-to-cluster range in surface density across our sample is  $\sim 0.5$  dex at almost all radii (and considerably less if Ph-I is excluded). Stochastic variations in individual profiles obscure any trend of profile shape with  $M_{200}$ , particularly for our most massive haloes; there is a weak trend of amplitude consistent with the expected correlation between  $M_*$  and  $M_{200}$  (see table 1). The central surface density ( $R < 10$  kpc) is notably lower in Ph-A (the oldest cluster) and an

<sup>4</sup> Our simulation does not include baryonic effects which could make the potential more spherical, so this elongation may be exaggerated.

<sup>5</sup> Throughout this paper we only consider profiles in circular apertures. Both Zibetti et al. (2005) and Seigar et al. (2007) find that changes in the profile of BCG ellipticity and position angle do not correspond directly to inflections in the surface brightness profile.



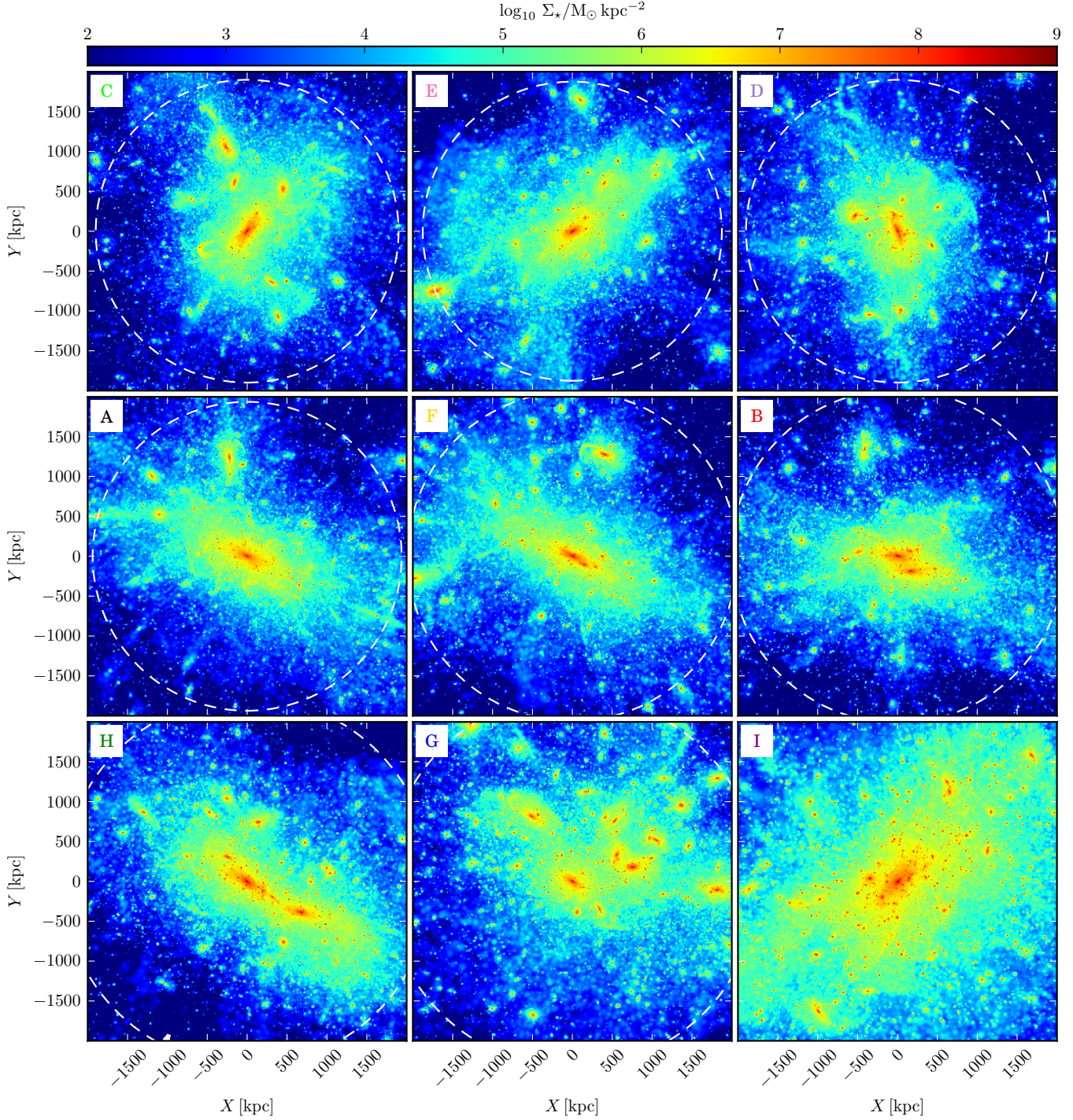


**Figure 1.** Projected  $3 \times 3$  Mpc images of the Phoenix clusters centred on their BCGs.  $M_{200}$  increases from left to right and top to bottom. The white dashed line shows  $R_{200}$  (outside the image for Ph-I). The viewing angle is chosen randomly. Colours correspond to stellar mass surface density on a  $\log_{10}$  scale. Particles are smoothed by a cubic spline kernel scaled by the density of their 64 nearest neighbours. ‘Hot spots’ are individual cluster galaxies; only very small scale density fluctuations are due to shot noise. The brightest galaxies are surrounded by extensive diffuse envelopes of tidal debris.

order of magnitude higher in Ph-H (the second youngest, which has a complex core structure). These differences hold for different random choices of projection, because projection effects are generally smaller than the scatter between our clusters. The largest differences between clusters and between different projections for any given cluster are at  $R < 10$  kpc, where neglecting the gravity of baryons makes our model less reliable in any case.

Accreted stars dominate over in situ stars (dotted lines) at almost all radii, including the most luminous central regions of the BCG – the notable exceptions are Ph-A and Ph-F (the two oldest clusters) in which the ratio is almost 1 : 1 within  $R < 5$  kpc. This dominance of accreted stars at all radii distinguishes BCGs in very massive clusters from those in haloes of  $M_{200} \lesssim 10^{14} M_{\odot}$ , where in situ stars typically dominate within  $\sim 10$  kpc at  $z = 0$  (see C13)



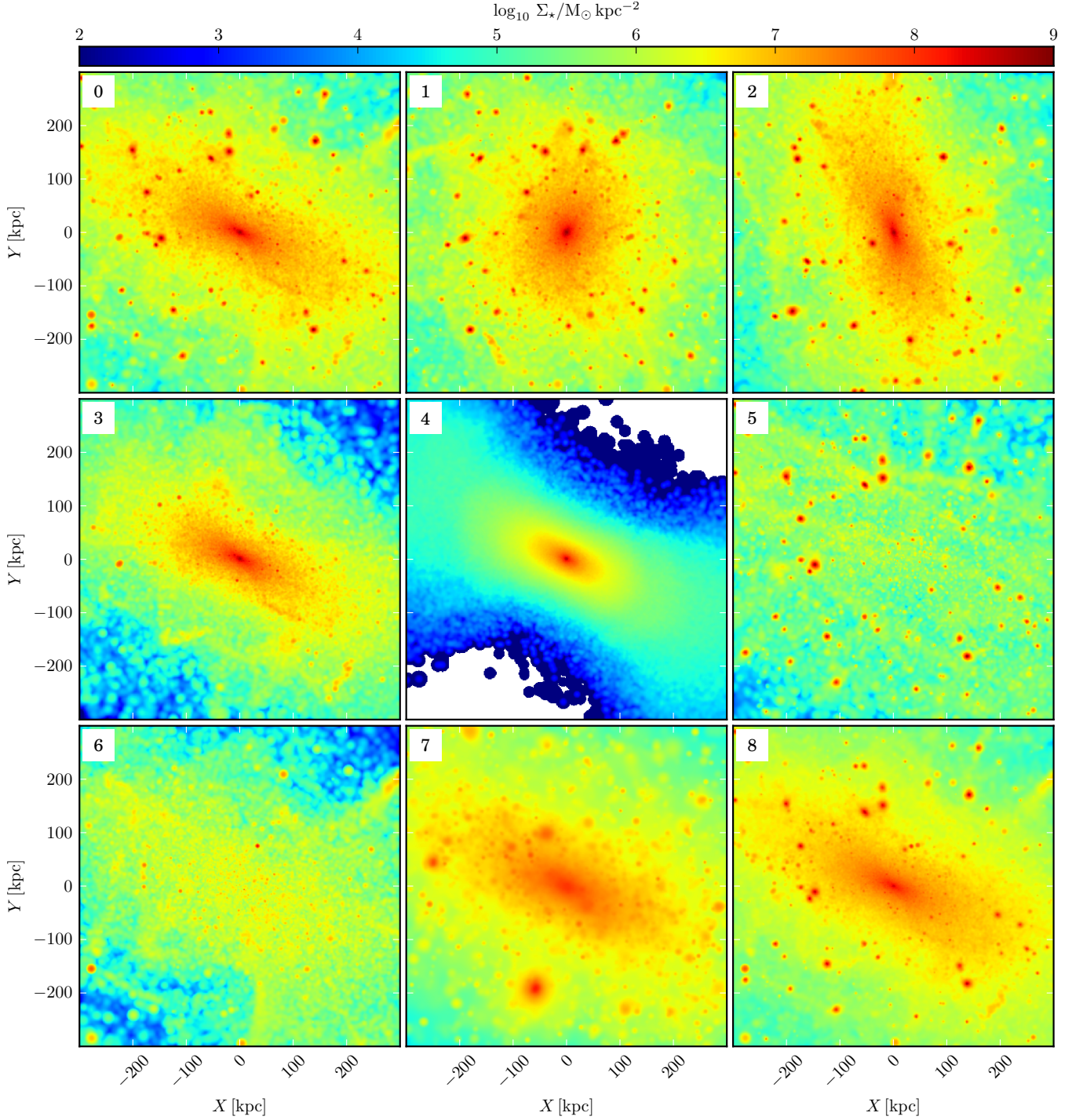


**Figure 2.** A zoom-in to the central  $300 \times 300$  kpc region of Ph-A, showing different subsets of particles in each panel. [0, 1, 2]: orthogonal projections of all stars (note triaxiality); [3] accreted BCG stars only (note absence of satellites, point-like overdensities are massive stellar particles and recently unbound stars); [4] in situ BCG stars only (note extent and elongation, due to halo response during last major merger); [5] all stars associated with surviving progenitor subhalos (bound and unbound; note coherent streams); [6] stars associated with ‘sub-resolution’ haloes that survive in the semi-analytic part of our model but not in the N-body simulation (by default in our model, all these stars are assigned to the BCG; note central concentration); [7] all stars at Phoenix level 4 resolution (see appendix A; trivial timing and orbit differences mean satellite positions are not identical; note convergence in density of BCG light); [8] all stars in an model with  $f_{\text{mb}} = 0.05$  (note slightly more diffuse centre of BCG).

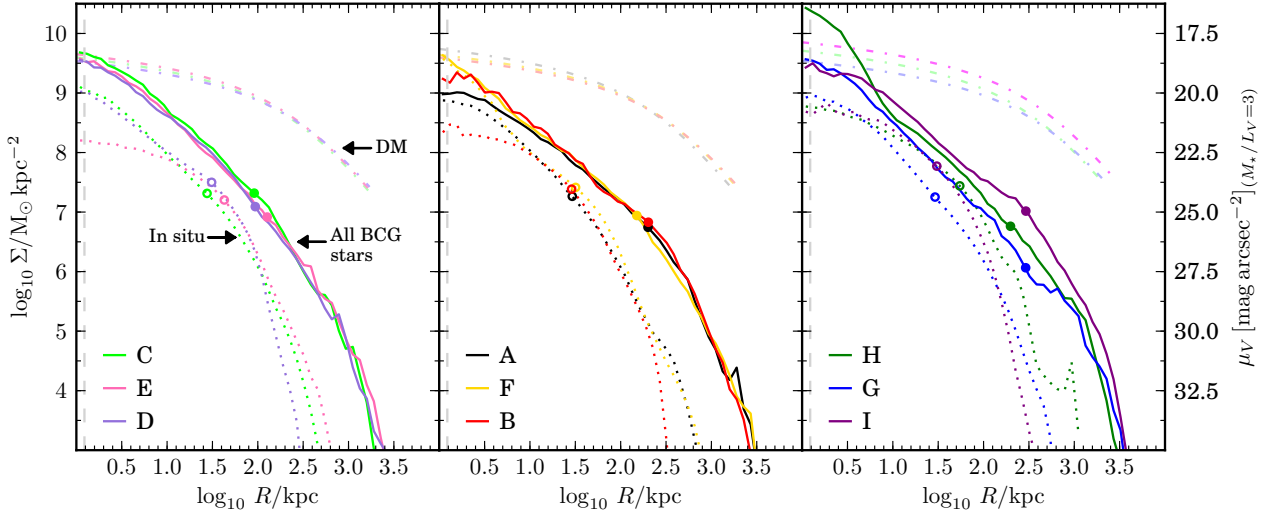


**Figure 3.** Surface density profiles of BCG stars in Phoenix clusters A–I (solid lines; simulations are ordered by  $M_{200}$ ). Dotted lines show the profiles for in situ stars only and dot-dashed lines plot the surface density of the best-fit NFW dark matter profile out to the virial radius (Gao et al. 2012). Filled and open circles mark the half-mass radii of the total and in situ profiles respectively ( $R_{50}$ ). A vertical grey dashed line indicates the simulation softening length. The right-hand axis gives an approximate conversion of  $\Sigma_*$  to  $V$ -band surface brightness, assuming  $M_*/L_V = 2.5$ . Clusters of similar mass have similar profiles, with accreted stars dominating at almost all radii.

and influence the total surface brightness profile significantly out to  $\sim 30$  kpc. It is also notable that the profiles of in situ stars in Fig. 3 typically have a similar shape to the total light profile – C13 found that this is not the case in less massive haloes. This indicates in situ stars and accreted stars are relatively well-mixed in the BCGs of massive clusters.

Our BCGs are an order of magnitude more massive than those studied at comparable resolution by C13. Their half-mass radii ( $R_{50}$ ; see table 2) nevertheless lie on an extrapolation of the trend shown in C13 for early-type galaxies above  $\sim 10^{11.3} M_\odot$ , suggesting no further steepening of this relation in the regime where size growth is dominated by accretion. This behaviour agrees roughly with the observed relations of Guo et al. (2009) and Bernardi et al. (2012), although our BCGs are  $\sim 0.2$  dex larger at a fixed stellar mass compared to an extrapolation of the SerExp relation preferred by Bernardi et al.. At the resolution of Phoenix, excluding stars from sub-resolution haloes does not affect this result significantly.

## 4.2 Comparison to observations

We now compare the amplitude and shape of our simulated BCG surface brightness profiles to observations. There are many deep BCG surface brightness profiles in the literature, covering a wide range of galaxy and halo masses (Schombert 1986, 1988; Uson et al. 1991; Mackie et al. 1990; Graham et al. 1996; Gonzalez et al. 2005; Patel et al. 2006; Krick et al. 2006; Krick & Bernstein 2007; Seigar et al. 2007; Bildfell et al. 2008; Donzelli et al. 2011). However, the majority of these are likely to correspond to clusters much less massive than those in the Phoenix sample. C13 found that the shape and amplitude of surface brightness profiles simulated with our technique are strongly correlated with  $M_{200}$ . A shallow  $M_*$ – $M_{200}$  relation means that comparison at fixed  $M_*$  introduces considerable scatter to these trends. Therefore, we choose observed clusters for comparison according to estimates of the total mass en-

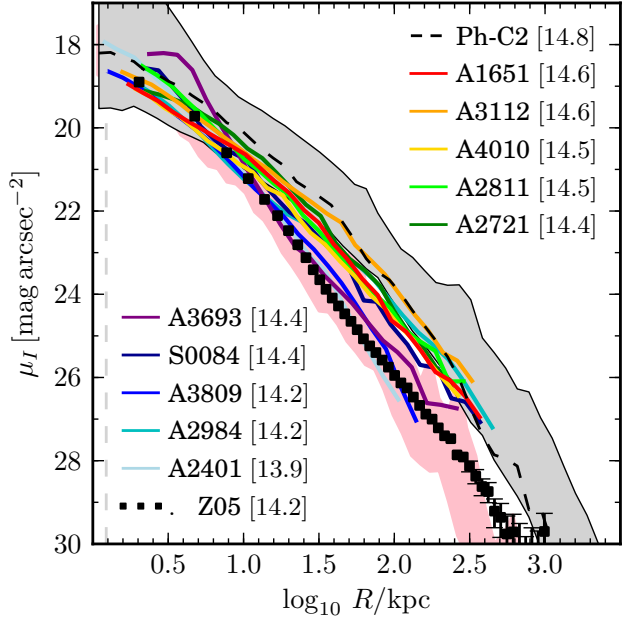


**Figure 4.** Envelope of simulated surface brightness profiles in Phoenix (grey region) and Millennium II ( $13.8 < \log_{10} M_{500}/M_\odot < 14.0$ , pink region) compared to observations in the Cousins  $I$  band from Gonzalez et al. (2005,  $+0.429$  mag to convert to AB, corrected for  $(1+z)^4$  SB dimming). The black dashed line shows one random projection of the least massive Phoenix cluster, Ph-C, for reference. The legend indicates Abell catalogue (A: North, S: South) and, in parenthesis, the MCXC  $\log_{10} M_{500}$  value from Piffaretti et al. (2011). Squares with error bars show the stacked BCG profile of Zibetti et al. (2005) in the SDSS  $i$  band (assuming  $i - I = 0.1$  mag). The shape and amplitude of simulated profiles and their trend with  $M_{500}$  agree well with these data.

closed within particular contours of overdensity (e.g. 500 times the critical density of the universe, denoted  $M_{500}$ ).

The precision of most cluster mass measurements is likely to be no better than  $\sim 25$  per cent and the absolute calibration can vary by even more between different studies (see Rozo et al. 2014 and Applegate et al. 2014 for recent discussions). Nevertheless, they become increasingly accurate for massive clusters where a variety of estimators can be applied, to the point where they are likely more reliable than surface brightness limited  $M_*$  measurements for BCGs. Moreover, cluster mass estimates are usually independent of the BCG surface photometry we wish to compare with (this is not the case for stellar masses; e.g. Bernardi et al. 2013). We obtain aperture mass measurements from the MCXC catalogue of Piffaretti et al. (2011), who standardised heterogeneous X-ray luminosity data to create a single catalogue of self-consistent  $M_{500}$  estimates.

In Fig 4 we show  $I$ -band surface brightness profiles from the catalogue of Gonzalez et al. (2005). Matching against MCXC yields 10 BCGs in common, of which 3 have  $\log_{10} M_{500}/M_{\odot} > 14.5$ . Our least massive Phoenix halo is Ph-C (profile shown by a black dashed line) which has  $\log_{10} M_{500}/M_{\odot} = 14.9$ . The envelope of the Phoenix profiles is indicated by a grey shaded region. The Gonzalez et al. (2005) profiles have similar amplitude to one another at 10 kpc,  $\sim 1$  mag arcsec $^{-2}$  below the mean of our simulations but within the lower envelope. The data have a weak trend towards steeper slopes at lower  $M_{500}$ , such that only the most massive (e.g. Abell 1651, Abell 3112) have shapes in good agreement with the simulations. The steeper slope and lower amplitude of profiles from less massive BCGs is, however, in good agreement with the 16 clusters of mass  $13.8 < \log_{10} M_{500}/M_{\odot} < 14.0$  simulated with the same technique by C13 (pink shaded region). We conclude that our models are consistent with the Gonzalez et al. (2005) data, given the systematically higher masses of the Phoenix haloes.

Fig 4 also shows data from Zibetti et al. (2005), who stacked SDSS  $i$ -band images of  $z \sim 0.25$  BCGs to derive an average surface brightness profile. These data are in agreement with the individual profiles of Gonzalez et al. (2005) for masses  $\log_{10} M_{500}/M_{\odot} \lesssim 14.2$  and with our Millennium II results. As noted in C13, this is consistent with estimates of the mean halo mass of the Zibetti et al. (2005) sample based on richness (Roza et al. 2009).

Fig. 5 presents a similar comparison to the Cousins  $R$ -band data of Donzelli et al. (2011), published as either one- or two-component fits to regions  $\mu_{R_c} > 24.5$  mag arcsec $^{-2}$ . Yellow and green shaded regions show the envelope of best-fit profiles for BCGs in this sample that can be matched to the MCXC catalogue in the mass ranges  $14.6 < \log_{10} M_{500}/M_{\odot} < 14.7$  (4 galaxies) and  $14.7 < \log_{10} M_{500}/M_{\odot} < 14.8$  (7 galaxies) respectively. These agree well with the Phoenix halos in the range of  $\mu_{R_c}$  used for the fit. Three galaxies from Donzelli et al. (2011) are plotted individually. Abell 2029 (red line) is the only cluster in Donzelli et al. matched to an MCXC cluster with  $\log_{10} M_{500}/M_{\odot} > 14.8$ . This most massive BCG agrees particularly well with our simulations. The fits for Abell 543 and Abell 2256 are very different to the other halos in their  $M_{500}$  range, suggesting either that those clusters are atypical, that there are issues with their photometry in Donzelli et al. (2011), or that their MCXC halo masses are greatly overestimated (by more than an order of magnitude according to the predicted trends of C13).

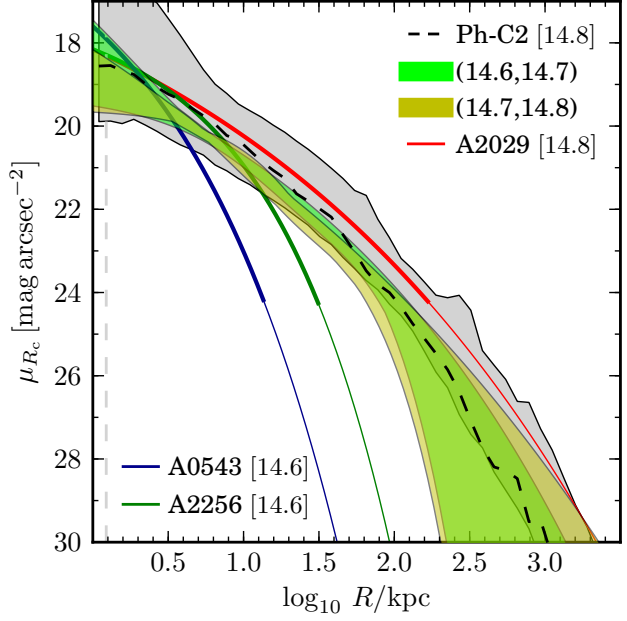


**Figure 5.** Comparison to observations in the  $R_c$  band from Donzelli et al. (2011, converted from Vega to AB by adding 0.117 mag and corrected for SB dimming). Shaded areas (green and yellow) are envelopes of best fit profiles for BCGs with MCXC masses  $14.6 < \log_{10} M_{500}/M_{\odot} < 14.7$  (4 galaxies, green) and  $14.7 < \log_{10} M_{500}/M_{\odot} < 14.8$  (7 galaxies, yellow). Two galaxies in the lower interval, (A0534 and A2256), have extremely concentrated profiles; we show these individually, with thinner lines where the fits are extrapolated. Abell 2029 (red line) is the only galaxy in Donzelli et al. (2011) with an MCXC mass  $\log_{10} M_{500}/M_{\odot} > 14.8$ . The Phoenix simulations also agree well with these data, except for the two outliers (compare Fig. 4).

Finally, Fig. 6 compares our simulations with the data of Bildfell et al. (2008) in either the CFHT/MegaCam  $r'$ -band or the CFHT/12K  $R$ -band. We select MCXC-matched clusters with  $\log_{10} M_{500}/M_{\odot} > 14.9$ . This sample should be well-suited to comparison with our simulations because several of the most massive clusters in the MCXC catalogue are included. However, given the good agreement with less massive clusters seen in previous figures, the discrepancies in Fig. 6 are surprising. The simulations overpredict the observed profiles by 1–2 magnitudes at 30 kpc.

Curiously, the approximate trend of amplitude with halo mass seen in the data of Gonzalez et al. (2007) is absent from the data of Bildfell et al. (and remains so if less massive cluster profiles in their sample are included). If significant errors in photometry<sup>6</sup> and  $M_{500}$  can be ruled out, the discrepancy in Fig. 6 may point to a systematic problem with our model – for example, the luminosity of simulated BCGs may increase too rapidly with  $M_{200}$ . This could also explain the apparent  $\lesssim 0.2$  dex excess of  $R_{50}$  at  $M_{200} \sim 10^{14} M_{\odot}$  in our simulations with respect to observed relations (see previous section and C13).

<sup>6</sup> Hubble Space Telescope (HST) photometry of Abell 2390 presented by Newman et al. (2013b) agrees very well (in shape) with the relatively steep profile of Bildfell et al. (2008). Newman et al. also obtain  $M_{500} \sim 10^{15.1} M_{\odot}$  based on weak and strong lensing, which makes the disagreement with our model marginally worse (see also Applegate et al. 2014).



**Table 2.** Fits to BCG stellar mass surface density profiles (listed in order of increasing  $M_{200}$ ). Following the halo label, columns show groups ( $R_{50}$  [kpc],  $\log_{10} \Sigma_{50}/M_{\odot} \text{ kpc}^{-2}$ ,  $n$ ) corresponding to the parameters of scale radius, surface density and Sèrsic index in equation 1. From left to right, these groups correspond to fits of a single De Vaucouleurs profile, a single Sèrsic profile, and a two-component Sèrsic profile. The latter is split into principle (1) and secondary (2) components according to their contribution to the total mass integrated over the radial range  $1 < R < 10^{3.5}$  kpc. The final column gives  $f_2$ , the mass fraction of the secondary component. See text for details of the constraints on each profile model.

Name	$R^{1/4}$			Single Sèrsic			Double Sèrsic (1)			Double Sèrsic (2)			$f_2$
	$R_{50}$	$\log_{10} \Sigma_{50}$	$n$	$R_{50}$	$\log_{10} \Sigma_{50}$	$n$	$R_{50}$	$\log_{10} \Sigma_{50}$	$n$	$R_{50}$	$\log_{10} \Sigma_{50}$	$n$	
C	87.2	7.28	4.00	107	7.15	4.09	144	6.89	3.23	9.46	8.41	4.48	0.14
E	64.8	7.39	4.00	117	7.00	4.64	60.0	7.38	4.96	377	5.77	1.66	0.37
D	135	6.85	4.00	128	6.95	3.29	179	6.65	2.51	15.0	7.93	4.56	0.15
A	181	6.64	4.00	189	6.71	3.29	215	6.63	2.77	6.86	8.24	4.81	0.05
F	148	6.85	4.00	156	6.84	3.87	191	6.67	3.19	7.84	8.34	4.34	0.08
B	93.9	7.17	4.00	132	7.02	3.39	263	6.49	0.96	75.6	7.14	6.53	0.47
H	169	6.89	4.00	196	6.81	3.74	98.2	7.16	6.97	646	5.71	0.624	0.34
G	48.3	7.42	4.00	309	6.04	9.07	217	6.25	9.55	819	5.11	0.501	0.23
I	179	7.04	4.00	279	6.87	3.35	515	6.51	1.52	46.7	7.74	3.69	0.18

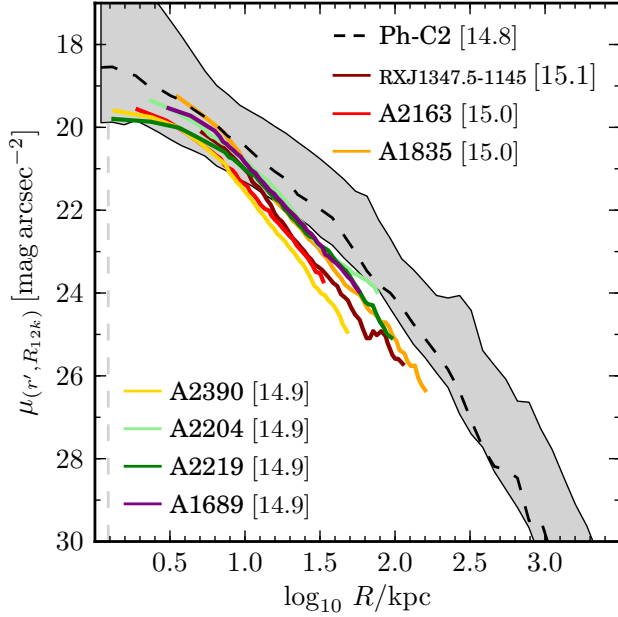


**Figure 6.** Comparison to observations in the MegaCam  $r'$  and CFHT 12K camera Mould  $R$  bands from Bildfell et al. (2008, converted from Vega to AB by adding 0.138 mag, and corrected for SB dimming; we assume no colour offset between these two filters). Galaxies were selected to have MCXC masses  $\log_{10} M_{500}/M_{\odot} > 14.9$ . The simulations do not match these data as well as those in previous figures; this could point to systematic errors in the photometry and/or  $M_{500}$ , or else to an overproduction of BCG stellar mass in our model (compare Fig. 4).

### 4.3 Functional forms

The so-called ‘cD envelope’ phenomenon (Matthews et al. 1964; Oemler 1976) refers to an ‘upturn’ in surface density relative to the extrapolation of a standard profile (often, but not strictly, an  $R^{1/4}$  law) fit to the high surface brightness regions of a BCG (e.g. Schombert 1988; Liu et al. 2008). The visual impression of these ‘haloes’ is particularly striking on deep photographic plates. Fig. 7 shows maximum likelihood  $R^{1/4}$  profile fits to our simulations in regions  $\Sigma_{\star} > 10^7 M_{\odot} \text{ kpc}^{-2}$ , corresponding to a surface brightness  $\mu_R \lesssim 26.5 \text{ mag arcsec}^{-2}$  (e.g. Seigar et al. 2007) and radii roughly  $R \lesssim 100 \text{ kpc}$ . Values of amplitude and scale radius for each halo are given in Table 2. Upward deviations from these fits at

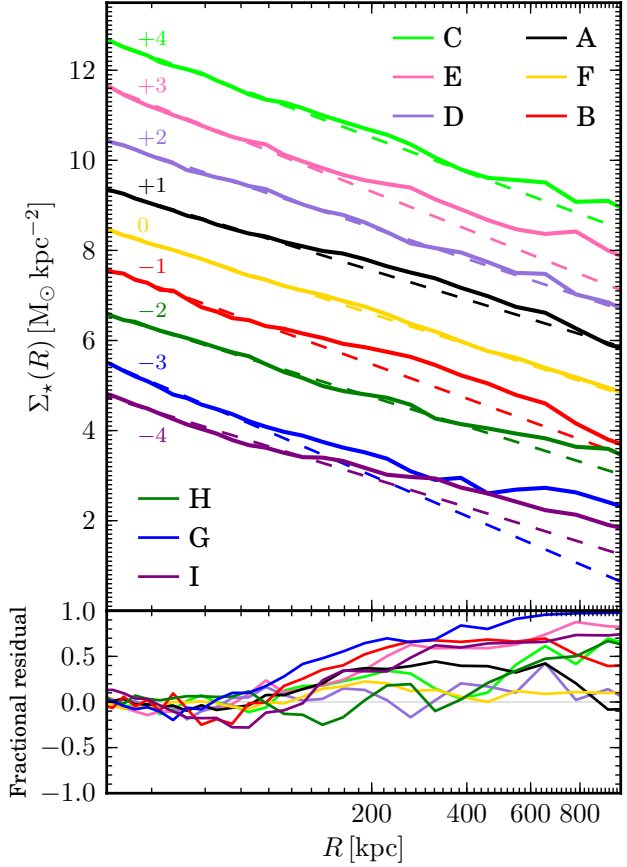


**Figure 7.** Surface mass density of BCG+ICL stars, with the  $x$ -axis scaled such that a  $\Sigma_{\star} \propto R^{1/4}$  profile is a straight line. For clarity, each profile is offset in  $\log_{10} \Sigma_{\star}$  by  $\pm 1$  to 4 dex as indicated ( $M_{200}$  increases in order from top to bottom). Dashed lines correspond to  $R^{1/4}$  fits to regions more dense than  $\Sigma_{\star} = 10^7 M_{\odot} \text{ kpc}^{-2}$ . Fractional residuals are shown in the lower panel. cD-like upturns relative to the inner  $R^{1/4}$  fit occur at  $R \gtrsim 200 \text{ kpc}$  in at least 5 clusters (A, B, E, G, I).

larger radii are prominent in halos B, E, G and I, and also apparent in A, C and H. Halos D and F show very little deviation from a

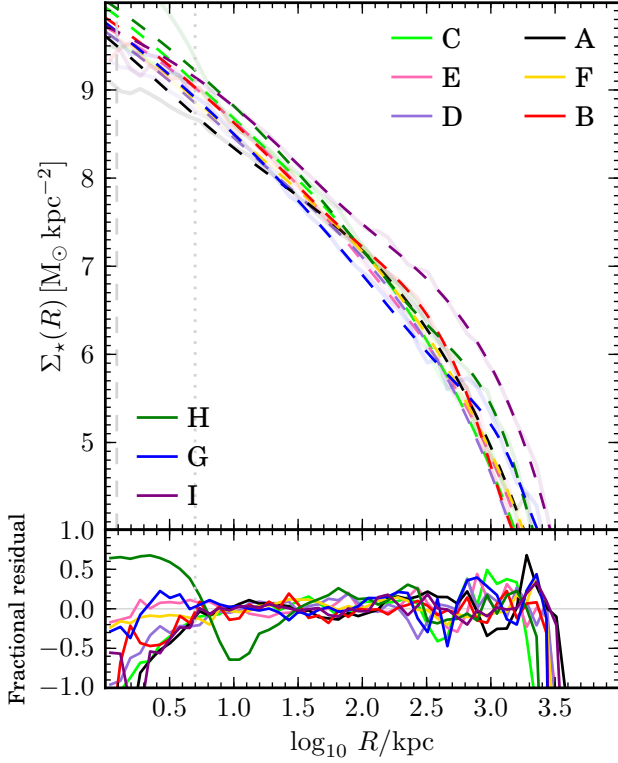


**Figure 8.** Upper panel: dashed lines are double Sersic profile fits to arbitrary projections of BCG+ICL stars over the range of radius and density shown in the figure. Simulation data are shown as faint solid lines of the same colour. Parameters are given in table 2. Lower panel: fractional residuals of each fit. These maximum likelihood fits assume a gaussian prior on  $\Sigma_*(R)$  at each data point, with a fiducial dispersion  $\sigma = 5\%$ , and exclude the innermost 5 kpc (dotted line). Double Sersic profiles fit well in the range 10 kpc to 1 Mpc; components with large half-mass radii tend to have  $n \lesssim 2$ .

single  $R^{1/4}$  law. There is, at most, a very weak trend of increasing excess with  $M_{200}$  or halo assembly time.

This ‘upturn’ simply reflects the now well-known fact that massive BCGs are not well fit by  $R^{1/4}$  profiles and does not reveal much about the physical significance of the ‘excess’ light (Lugger 1984; Seigar et al. 2007; Schombert 2013). The more general Sersic function

$$\Sigma(R) = \Sigma_{50} \exp\{-b_n[(R/R_{50})^{1/n} - 1]\} \quad (1)$$

provides a much better description of the surface brightness of elliptical galaxies over a wide range in luminosity (Graham & Driver 2005). Here  $\Sigma_{50} \equiv \Sigma(R_{50})$  is the amplitude of the profile at  $R_{50}$ , the radius enclosing half the mass (or light) in projection, and  $n$  is the Sersic index, which sets the concentration of the profile ( $n = 4$  corresponds to an  $R^{1/4}$  profile and  $n = 1$  to an exponential profile). C13 found that  $R_{50}$  and  $n$  for the central galaxies of massive haloes in their simulation matched observations well – both parameters were found to increase systematically with halo mass. For massive elliptical galaxies, the increase in size and Sersic index with mass is driven by accretion, as in the models of Cole et al. (2000) and Naab et al. (2009). The Phoenix BCGs represent extreme examples of these trends – not only are they more massive and dynamically younger than other elliptical galaxies, but almost all of their stars are accreted. This results in large sizes and high Sersic indices.

Single Sersic functions are a reasonable first order descrip-

tion of the BCG+ICL stellar mass surface density profile in all nine Phoenix clusters, but they are far from perfect. The parameters of maximum likelihood Sersic fits are given in Table 2. For these fits, we excluded the inner 5 kpc, because numerical softening dominates at  $\lesssim 1$  kpc and because we neglect the gravity of baryons, which is likely to be a poor approximation in that region<sup>7</sup>.

A number of authors, in particular Seigar et al. (2007), advocate fitting observed BCG profiles with the sum of two Sersic components; the outer component was found to have an exponential form ( $n \sim 1$ ) in many cases (see also Donzelli et al. 2011). Fig. 8 and columns 8–13 of table 2 show the results of double Sersic fits to our simulations, with the constraints given above. The residuals for these fits are  $\lesssim 50\%$  over three orders of magnitude in radius. In five cases (Ph-B, E, G, H and I) we find that the Sersic component with larger half-mass radius (all  $\gtrsim 250$  kpc) has  $n \lesssim 2$  (for Ph-G and Ph-H,  $n < 1$ ). The haloes with exponential outer components are also, perhaps not surprisingly, those with the strongest cD-like departures from  $R^{1/4}$  profiles. These simulation results provide a possible explanation for the exponential outer components found by Seigar et al. (2007) and Donzelli et al. (2011).

C13 concluded that double Sersic profiles are also an excellent fit to the average profile of central elliptical galaxies in haloes  $M_{200} \lesssim 10^{14} M_\odot$ . However, there is an important difference between that statement and our conclusions regarding the most massive BCGs. C13 showed that the double Sersic form in their central galaxies was due to the gradient in the ratio between in situ stars (dominant at  $R \lesssim 100$  kpc) and accreted stars. In contrast, as we show in the next section, the double Sersic form of the Phoenix BCGs is driven by a transition between *different accreted components*, in different states of dynamical relaxation and/or symmetry around the BCG. The transition between in situ and accreted stars is much less conspicuous.

## 5 SURFACE DENSITY SUBSTRUCTURE

Previous figures have shown that the azimuthally averaged surface density profiles of accreted stars in the BCGs of massive clusters have similar shape and amplitude. We now investigate why this is the case. We start from the fact that a BCG density profile can be considered as the superposition of many profiles, each corresponding to stars accreted from a single progenitor<sup>8</sup> galaxy.

### 5.1 Surface brightness of debris components

Fig. 9 shows the stellar mass of stripped debris that each individual progenitor contributes to the BCG, in rank order. The largest (rightmost) step in each of the curves in Fig. 9 corresponds to

<sup>7</sup> Observers also exclude the central regions when fitting surface brightness: Seigar et al. (2007) excluded the innermost 2–5 kpc to avoid regions dominated by PSF deconvolution, and Zibetti et al. (2005) excluded the inner 10–20 kpc. Since these profiles are concentrated, the size of the excluded region can influence the ratio of components in a double Sersic fit.

<sup>8</sup> For this section, the progenitor of a given star particle is the dark matter halo (or subhalo) to which it was last bound before joining the main branch of the cluster merger tree. Each of these progenitor halos is the root of its own merger tree and hence will contain stars formed in many different galaxies. Note that the mass contributed by a progenitor to the BCG need not equal the mass of the progenitor; many of the most significant progenitors survive and retain a significant fraction of their stellar mass at  $z = 0$ .

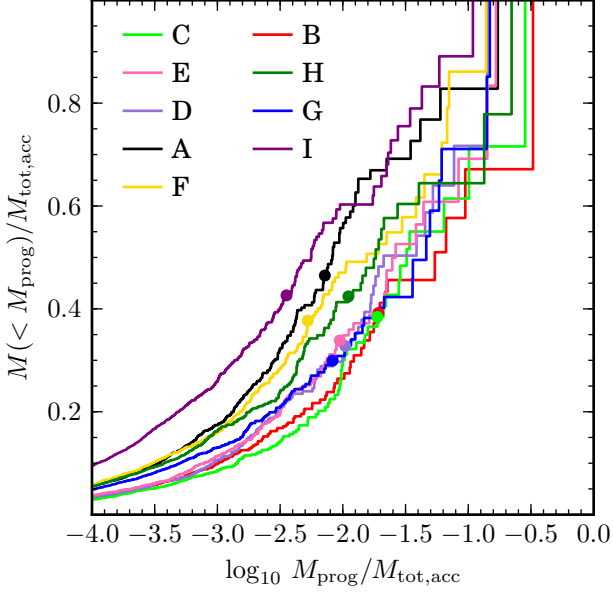


**Figure 9.** Distribution of progenitor stellar mass contributions for each Phoenix BCG, showing the fraction of the total accreted stellar mass,  $M_{\text{tot,acc}}$  (vertical axis), from systems with stellar mass,  $M_{\text{prog}}$  less than a given fraction of  $M_{\text{tot,acc}}$  (horizontal axis). The large steps at high  $M_{\text{prog}}$  correspond to the most massive contributions from individual progenitors. Dots mark the mass fraction corresponding to  $N_{\text{prog}}$ , an indication of the number of significant progenitors (see text and table 1). The Phoenix BCGs have many more significant progenitors than the less massive galaxies studied in C13 and Cooper et al. (2010).

the largest single contribution, which accounts for only 10–35 per cent of the total accreted stellar mass ( $M_{\text{tot,acc}}$ ). Most progenitor galaxies contribute much smaller fractions.  $N_{90}$ , the number of progenitors taken in decreasing mass order required to account for 90 per cent of  $M_{\text{tot,acc}}$ , spans the range  $61 \leq N_{90} \leq 657$  (Table 1). Cooper et al. (2010) took the square root of the second moment of the distribution in Fig. 9 (labelled  $N_{\text{prog}}$ ) as representative of the number of ‘significant’ progenitors. For our clusters we find  $8 \lesssim N_{\text{prog}} \lesssim 43$ . Depending on the halo, 50–70 per cent of  $M_{\text{tot,acc}}$  is accounted for by these significant progenitors, with individual masses  $M_{\text{prog}} \gtrsim 0.3$ –3 per cent of the total (hence roughly  $\gtrsim 10^{11} M_{\odot}$  each).  $N_{\text{prog}}$  is therefore larger for massive clusters than for the stellar haloes of Milky Way-like systems, where the bulk of accreted mass is contributed by fewer than five progenitors, typically with only one or two dominating (Cooper et al. 2010).

The top panel of Fig. 10 shows how the overall accreted density profile is built up by these contributions, using Ph-E as an example (the bottom panel is discussed in section 5.2). Separate profiles are shown for debris from each of the top 8 most massive progenitor galaxies (which make up  $\sim 60$  per cent of the accreted mass according to Fig. 9). Two types of profiles can be distinguished in this figure. The profiles of stars from the two most massive progenitors (labelled 1 and 2) are centrally concentrated, with similar shapes that resemble the overall profile. Debris clouds from the other progenitors have much larger effective radii, lower concentration (Sersic index) and hence very little mass within  $R \lesssim 100$  kpc. In the case of progenitor 8, the debris is concentrated almost entirely in one radial bin at  $\sim 800$  kpc.

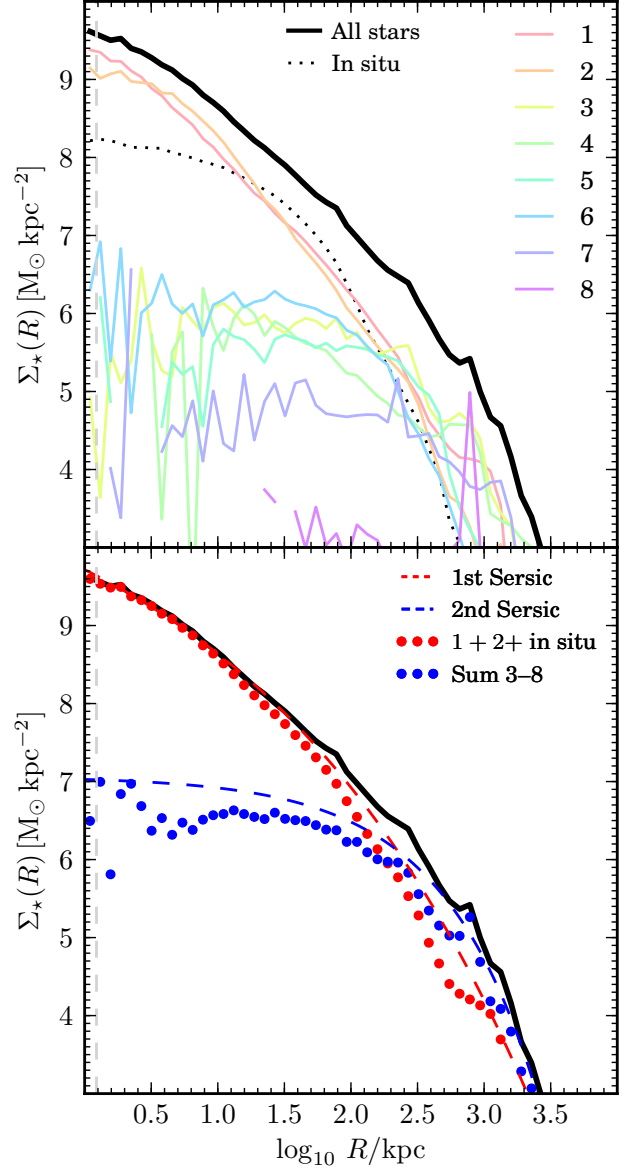


**Figure 10.** Decomposition of the stellar mass surface density profile of Ph-E (thick black line) into components corresponding to the 8 accreted systems that contribute most mass to the BCG/ICL (thin coloured lines, labelled in rank order of stellar mass contributed, from 1 to 8). The in situ component is shown by the black dotted line. In the bottom panel, red and blue dashed lines show the components of a double Sersic fit to the total stellar density profile. A vertical grey dashed line marks the softening length.

Fig. 11 shows images of each component, which help to explain the differences between their profiles. Components 1 and 2 are centrally concentrated and have a smooth distribution in projection, with only faint asymmetric structure to suggest they were accreted. These two galaxies fell into the cluster at  $z \approx 1.0$  and  $z \approx 1.8$  respectively. Component 1 was disrupted very rapidly, although a very small remnant core survives as a subhalo at  $z = 0$  (marked by a red cross). Stars were stripped more gradually from component 2 over a period of 4 Gyr, but no core survives at  $z = 0$ . Together these progenitors contribute  $\sim 30$  per cent of the accreted stellar mass.

The progenitors of components 3, 4 and 5 fell into the clus-



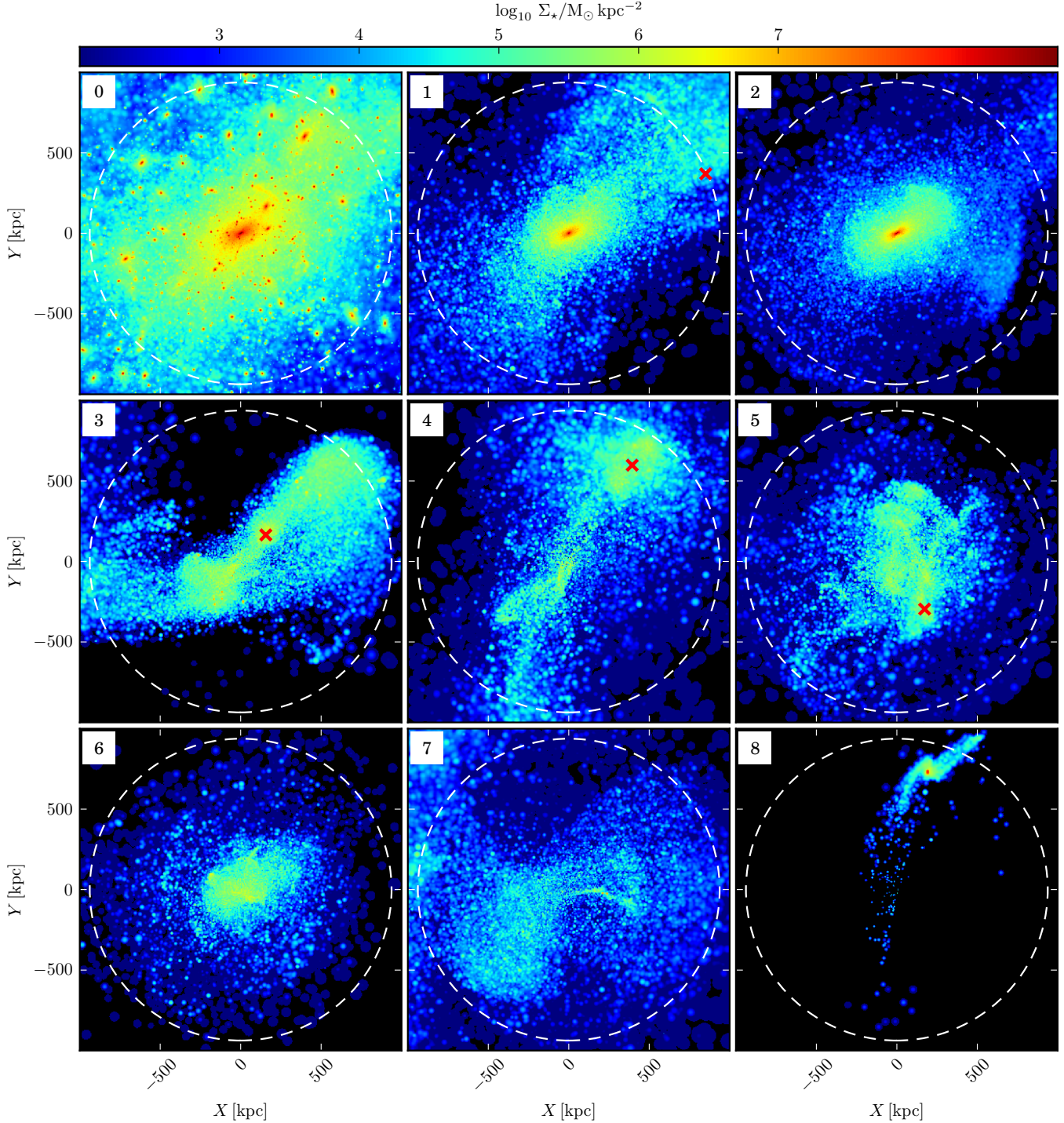


**Figure 11.** Surface mass density images as in Fig. 1 for stars associated with each of the top 8 accreted components in Ph-E (labelled from 1 to 8 in order of mass contributed). The white dashed circle shows  $\frac{1}{2} R_{200}$ . Red crosses mark the centre of the parent subhalo of each progenitor in cases where it survives. Panel 0 shows the total surface density of all stars. The most significant debris components cover a wide range in terms of central concentration, symmetry and dynamical relaxation.

ter at redshifts  $0.7 < z < 1.4$ , but were stripped more recently ( $z \lesssim 0.5$ ), with only half of the stars they contribute to the BCG being stripped earlier than, respectively, 2 Gyr, 2 Gyr and 5 Gyr ago. The progenitor of component 3 spent nearly 6 Gyr in the cluster potential before losing any stars to tidal stripping. All these components have an unrelaxed morphology, with debris tracing stream-like orbits. Component 3 shows the early stages of radial shell for-

mation (Cooper et al. 2011) and component 5 traces a rosette-like orbit, seen edge-on in this projection. Each of these components is associated with a surviving resolved subhalo at  $z = 0$ . Unlike the inconspicuous remnant core of progenitor 1, these subhaloes correspond to some of the most luminous cluster members in the top left panel of Fig. 11.

Progenitor 6 fell in and was disrupted over a similar timescale



to progenitor 2. Although its debris appears quite uniformly distributed it is much less centrally concentrated. The diffuse shell-like debris of progenitor 7 is the result of very rapid disruption (over  $\lesssim 1$  Gyr) after infall at  $z \sim 0.7$ . Neither progenitor survives at  $z = 0$ . Finally, progenitor 8 appears very much like an intact galaxy with tidal tails. This is partly a projection effect; most of these stars are turning around in a ‘kink’ at the apocentre of a complex, approximately figure-of-eight orbit, the plane of which is almost perpendicular to the line of sight. Despite their concentration, the dark matter particles tagged with stars from this progenitor are assigned to the main halo by SUBFIND. This relatively massive galaxy is identified as a ‘survivor’ with a sub-resolution halo in our semi-analytic model, making this one of the rare cases where the particles from such a galaxy are still confined to a small region in configuration space.

We conclude that the different profiles of the debris components reflect a range of possibilities for how progenitor galaxies can be disrupted, varying according to their mass, accretion time and orbit. We can infer that centrally concentrated profiles with high Sèrsic index correspond to systems that sink (rapidly) to the centre of the cluster and/or that are accreted at  $z \gtrsim 1$ . These tend to include at least some of the most massive progenitors: components labelled 1, 2 and 6 in the above figures are ‘major’ mergers, having stellar mass ratios with the BCG of  $\sim 1 : 3$  at infall. Such mergers are likely to result in violent relaxation. Extended, diffuse profiles generally correspond to galaxies with higher mass ratios (in the examples above, all  $1 : 10$  or higher) disrupted in the cluster outskirts, possibly (but not necessarily) on orbits with higher angular momentum. Longer dynamical times naturally preserve structure in recently accreted debris at larger radii, such as streams and shells. In general, the massive debris components associated with diffuse profiles are also visually ‘unrelaxed’, although the degree of visual substructure is not always obvious from the concentration or smoothness of the profile.

We find different relative proportions of ‘relaxed’ and ‘unrelaxed’ components among the most significant progenitors across our 9 simulations. In general, however, progenitors with diffuse profiles dominate the outskirts and smooth concentrated profiles dominate in the centre of the cluster, as in the example shown. Individual counterexamples are not hard to find – dynamically young structures can be found in the centre of some clusters, and there is an appreciable net contribution at large radii from components with a ‘smooth’ spatial distribution.

## 5.2 Physical origin of double Sèrsic profiles

We now return to the meaning of the two components picked out by a double Sèrsic fit to the total surface density in section 4.3. These are shown for Ph-E by red and blue dashed lines in the bottom panel of Fig. 10. Their mass ratio is approximately 2:1, with the more concentrated component (red line) being the more massive. The transition between the two at  $\sim 200$  kpc corresponds roughly to the departure from an  $R^{1/4}$  law in Fig. 7 (the inner component has  $n \approx 5$ ). We see a clear similarity between these two components and the sum of the profiles of the ‘relaxed’ and ‘unrelaxed’ progenitor profiles respectively. We conclude that the large-scale inflection in the shape of the overall profile results from a transition between inner regions dominated by ‘relaxed’ accreted components and outer regions dominated by ‘unrelaxed’ accreted components. In Ph-E, this transition is picked out, approximately, by the double Sèrsic fit.

This result holds across our sample of 9 halos, even though

decompositions of the density profile show a different mix of relaxed and unrelaxed sub-components in each case. Where a double Sèrsic profile is not strongly favoured over a single Sèrsic (e.g. Ph-C, Ph-F), plots equivalent to Fig. 10 show a continuum of profiles, varying from ‘relaxed’ to ‘unrelaxed’ with increasing radius. Where a double Sèrsic fit is strongly favoured, the component with larger effective radius and lower Sèrsic index provides a reasonable estimate of the cumulative contribution of ‘unrelaxed’ accreted debris.

Substantial mass in one or more ‘unrelaxed’ debris components appears to be the origin of ‘cD envelopes’ in our simulated clusters. In particular, the diffuse light around other very massive galaxies in the cluster is responsible for the majority of the strong ‘cD envelope’ effect seen in halos Ph-B, Ph-G and Ph-H. The distorted outer envelopes of these bright cluster members (see Fig. 1) are not concentric with the BCG, hence their contributions to the overall profile are less concentrated (i.e. have lower Sèrsic index) when measured in BCG-centred apertures. In Ph-E and Ph-I, on the other hand, the envelope is not dominated by a single progenitor and is concentric with the BCG. The choice of the BCG can be ambiguous during cluster mergers. When several BCG candidates lie near the centre of an unrelaxed cluster, as in Ph-B and Ph-G, their envelopes may be much larger than their separation and hence the projected centroid of the diffuse light might not correspond to any of the brightest galaxies.

## 6 ICL FRACTION

The fraction of the stellar mass of a cluster made up by intracluster stars has been studied by many authors (e.g. Thuan & Kormendy 1977; Bernstein et al. 1995). This measurement depends sensitively on the nature of the BCG and ICL density distribution. Recent observational estimates of the ‘ICL fraction’ range from 10 to 50 per cent (Gonzalez et al. 2007; McGee & Balogh 2010; Sand et al. 2011). This wide range may be the result of lumping together very different sample selections (cluster and galaxy masses) and definitions of ICL, alongside scatter caused by observational uncertainties and stochastic variations between clusters (as discussed by Lin & Mohr 2004). We compare our simulations with Zibetti et al. (2005) and Gonzalez et al. (2007), because both these studies are based on large, well-defined samples of galaxies and do not depend strongly on assumptions about the nature or distribution of the ICL component.

Fig. 12 plots data from Gonzalez et al. (2007), who measured the ratio between the combined mass of the BCG and ICL (which we call  $M_{\star\text{BCG}}$ ) and the total stellar mass within  $R_{200}$ ,  $M_{\star,200}$  (this includes stars in satellite galaxies)<sup>9</sup>. Our Phoenix cluster simulations cover a range  $15 < M_{\star\text{BCG}}/M_{\star,\text{tot}} < 40$  per cent and therefore agree well with the spread of the Gonzalez et al. data at comparable  $M_{200}$ . If stars associated with sub-resolution haloes are treated as bound to satellites rather than the BCG, the Phoenix BCG stellar mass fractions are reduced by  $\lesssim 0.2$  dex.

Gonzalez et al. find a trend with  $M_{200}$ , such that the BCG and

<sup>9</sup> We are grateful to A. Gonzalez for providing measurements in an aperture of  $R_{200}$  rather than  $R_{500}$  as given in Gonzalez et al. (2007); halo masses have been scaled assuming an NFW concentration of 5, hence by a factor  $M_{200}/M_{500} = 1.38$ .

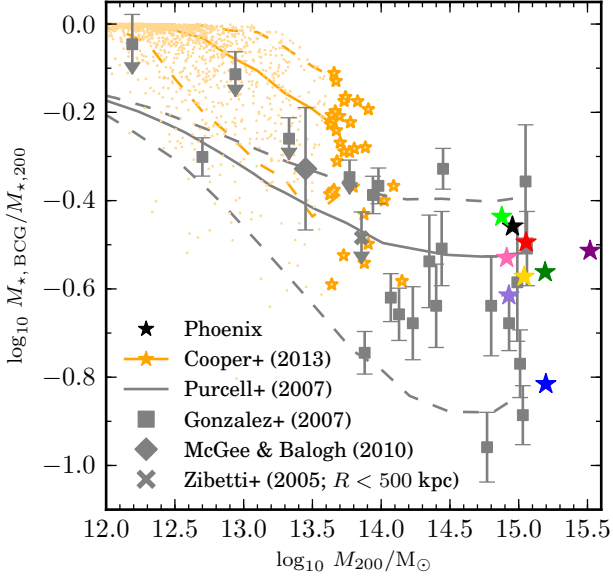


**Figure 12.** Stellar mass of central galaxies in our models (with no separation of ICL) as a fraction of the total stellar mass within  $R_{200}$  (this total mass includes all satellite galaxies). Filled star symbols correspond to the individual Phoenix haloes with our fiducial model that includes stars from sub-resolution semi-analytic halos in the BCG+ICL. Orange points show galaxies in Millennium II from C13; individual haloes of  $M_{200} > 10^{13.5} M_{\odot}$  are highlighted with orange star symbols. Orange lines show the median (solid) and 10–90 per cent range (dashed) of the Millennium II data. Grey points show observational data from Gonzalez et al. (2007, squares, assuming  $M_*/L = 3.6$ ), Zibetti et al. (2005, cross) and McGee & Balogh (2010, diamond). Arrows indicate measurements in an aperture of  $R < R_{200}$ , hence upper limits. Grey lines show the median and 10–90 per cent range for the model of Purcell et al. (2007).

its stellar halo account for  $\sim 50$  per cent of the total stellar mass at  $M_{200} \sim 10^{13.5} M_{\odot}$  (although see Balogh et al. 2008). McGee & Balogh (2010) obtained a similar value based on observations of intergalactic supernovae in galaxy groups ( $M_{200} \sim 10^{13.5}$ , black circle; see also Gal-Yam et al. 2003; Sand et al. 2011). Zibetti et al. (2005) found a mass fraction of 33 per cent in haloes of average mass  $\sim 7 \times 10^{13} M_{\odot}$ . These measurements are for haloes much less massive than those of Phoenix, so Fig. 12 compares them with the Millennium II results of C13 (orange stars and lines). At  $M_{200} = 10^{13.5} M_{\odot}$  we find a median value of  $M_{*,BCG}/M_{*,200} = 0.6$ , broadly consistent with the data but implying a more gradual decline with increasing  $M_{200}$ . Improving the statistics of observations in this mass range (for example through stacking; Cooper et al. 2013; Budzynski et al. 2014; D’Souza et al. 2014) would be beneficial, as would further simulations of low-mass galaxy clusters ( $10^{13} < M_{200} < 10^{15} M_{\odot}$ ).

Purcell et al. (2007) used simple scaling relations to populate haloes from an N-body simulation with stars and followed their merging histories to infer ‘BCG+ICL’ stellar mass fractions (see also Lin & Mohr 2004; Conroy et al. 2007). Their predictions for the distribution of  $M_{*,BCG}/M_{*,tot}$  and its variation with  $M_{200}$  are shown by the grey lines in Fig. 12. The Purcell et al. model agrees with our direct simulations at  $M_{200} \gtrsim 10^{14.5} M_{\odot}$  but predicts a substantially smaller fraction of stellar mass in the BCG at  $M_{200} \lesssim 10^{13.5} M_{\odot}$ . Although this is compatible with one data point of Gonzalez et al. (2007), Abell 3166, it is inconsistent with observations of the Milky Way and M31 (and similar galaxies),

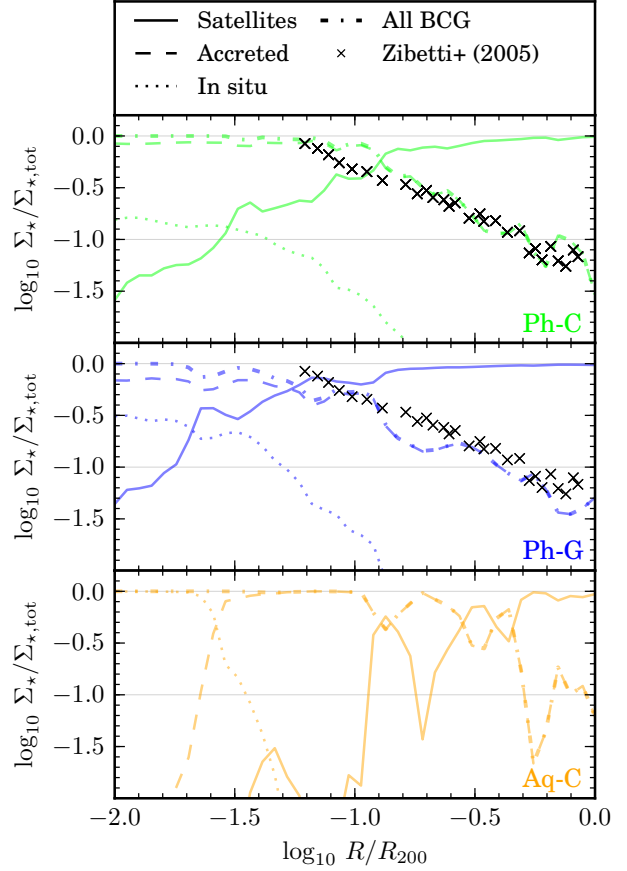


**Figure 13.** Surface mass density fraction of stars in the BCG (subdivided into accreted and in situ) and satellites, for haloes Ph-C (top) and Ph-G (middle). Crosses show the measurement of ICL mass fraction by Zibetti et al. (2005). Satellite stars account for most of the stellar mass beyond  $0.1 R_{200}$  and a large fraction at smaller radii. The lower panel compares to one of the Aquarius Milky Way-mass halos (Aq-C), in which the central galaxy and its stellar halo dominate out to  $0.5 R_{200}$ .

which have relatively well constrained halo masses and BCG+ICL fractions of  $\gtrsim 90\%$  (Li & White 2008; Helmi 2008; McConnachie 2012; Martínez-Delgado et al. 2010). In this respect the Millennium II results of C13 are more consistent with the data.

### 6.1 Radial variation

Fig. 13 shows how  $M_{*,BCG}/M_{200}$  varies with radius for haloes Ph-C and Ph-G (dot-dashed lines). Radii are expressed as a fraction of  $R_{200}$ . We break each of these curves into separate components representing in situ BCG stars (dotted lines), accreted BCG stars (dashed lines) and stars in satellite galaxies (solid lines).

In Ph-C, BCG stars account for more than 90 per cent of the stellar mass projected in annuli  $R \lesssim 0.1 R_{200}$ ; their contribution falls to  $\sim 3$  per cent at  $R_{200}$ . These findings hold on average for the nine clusters, with scatter comparable to the fluctuations in individual profiles. As a result, all the simulations (except Ph-G, see below) are in very good agreement with the average behaviour of the Zibetti et al. (2005) stack of BCGs (crosses). This agreement is remarkably insensitive to the  $\sim 1.5$  dex variation in  $M_{200}$  across our sample.

For comparison, the lower panel of Fig. 13 shows a high-

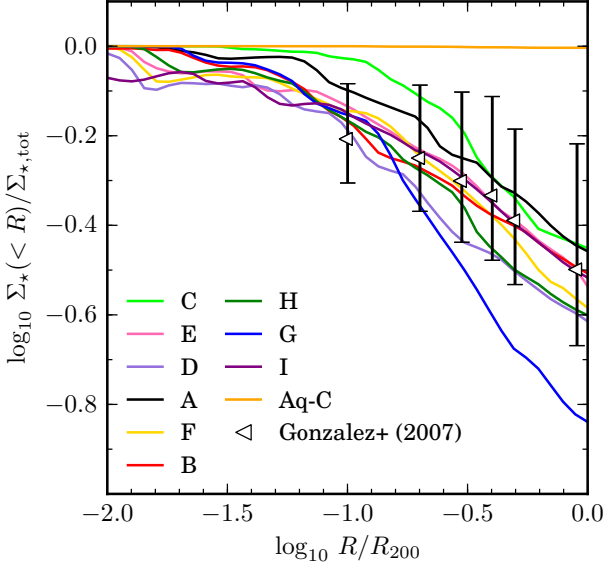


**Figure 14.** The *cumulative* enclosed mass fraction in BCG+ICL stars at different radii. Triangles show data from Gonzalez et al. (2007); solid lines show the same in Phoenix. The orange line corresponds to Aquarius Milky Way-mass Aq-C, in which the central galaxy and its halo dominate the total mass.

resolution simulation of a Milky Way-like halo analogue with  $M_{200} \sim 10^{12} M_{\odot}$  (Aquarius-C-2, Cooper et al. 2010). The trends in the individual components are similar to those in BCGs, with satellite stars dominating the projected mass at radii beyond 10 per cent of  $R_{200}$ . However, the Aquarius profile shows much larger oscillations due to individual stellar streams and satellites. Even though satellite stars dominate locally over  $\sim 50$  per cent of the projected area within  $R_{200}$ , they account for  $\lesssim 10$  per cent of the total stellar mass, as shown in Fig. 12.

Finally, in Fig. 14, we examine the *cumulative* value of  $M_{\star, \text{BCG}}/M_{\star, \text{tot}}$  within a given fraction of  $R_{200}$ . We find good agreement with the data of Gonzalez et al. (2007), who also found that the value of this ratio at any given fraction of  $R_{200}$  scales with cluster velocity dispersion (their figure 5). Fig. 14 supports such a trend in our models, albeit weakly, despite our  $M_{200}$  range being narrower than that of Gonzalez et al..

Ph-G deviates most from the average behaviour of  $M_{\star, \text{BCG}}/M_{\star, \text{tot}}$  in Figs. 12, 13 and 14. The latter two figures show that the ratio of BCG stars to satellite stars is lower at all radii compared to the observational average of Zibetti et al. (2005). Several of our haloes have comparable or higher satellite mass fractions in their inner regions, hence it is the low BCG mass ratio at  $R \gtrsim 0.1R_{200}$  that makes Ph-G an outlier in Fig. 12. Inspection of table 1 shows that the ratio of BCG stellar mass to total halo mass,  $M_{\star, \text{BCG}}/M_{200}$ , is particularly low in Ph-G, so it appears to be ‘missing’ stellar mass from its outer regions.

The most obvious reason for this deficiency is that Ph-G is dynamically very young. It is essentially two clusters in one halo (see Fig. 1), where the massive satellites have yet to suffer the full effects of the newly combined dark matter potential and the two BCGs have yet to merge (see also Dolag et al. 2010). As yet, however, there is little direct evidence for recent mergers driving the scatter in the observations plotted in Fig. 12. Of the three most comparable data points of Gonzalez et al. (2007) in Fig. 12, Abell clusters 2721 and 3705 have no dominant BCG (i.e. Bautz-Morgan

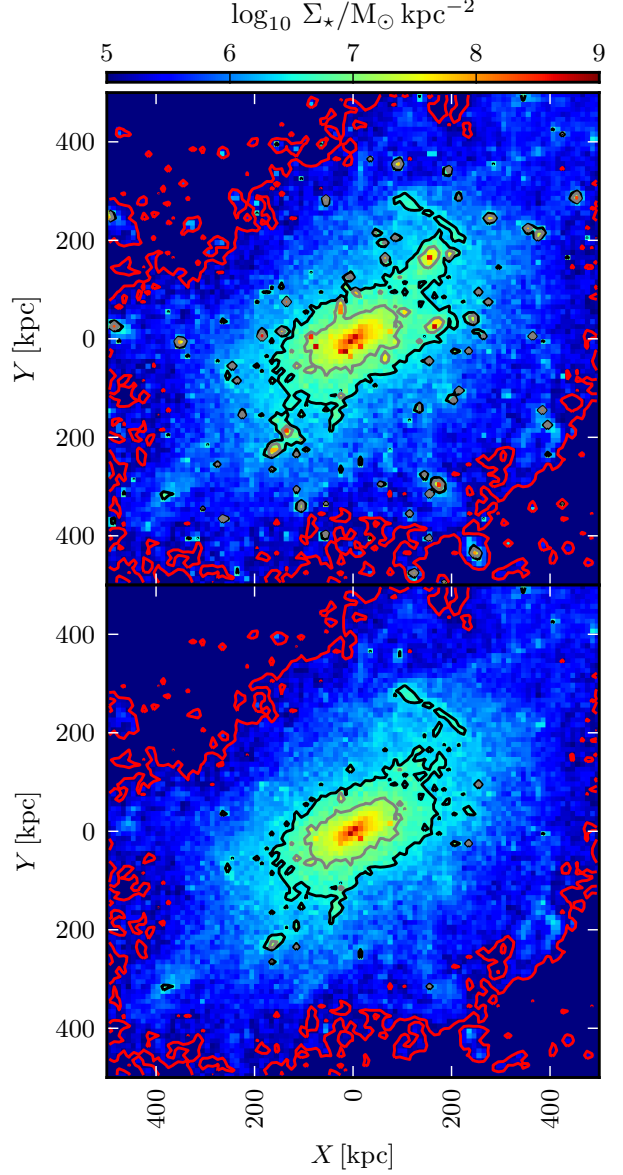


**Figure 15.** Central region of Ph-E at a resolution of  $1 \text{ kpc}^2$  per pixel. Contours mark stellar mass surface densities  $10^5$  (red),  $10^{6.5}$  (black) and  $10^7$  (grey)  $M_{\odot} \text{ kpc}^{-2}$ . The top panel shows all stellar mass in the simulation, including cluster members other than the BCG. In the bottom panel, only BCG stars are shown. BCG stars drive the orientation, extent and amplitude of the diffuse light at  $\Sigma \lesssim 10^{6.5} M_{\odot} \text{ kpc}^{-2}$ .

type III) and Abell 3750 also has a strongly bimodal X-ray morphology (Sivanandam et al. 2009), both of which are suggestive of unrelaxed clusters. Abell 1651, however, has symmetrical X-ray contours and Bautz-Morgan type I-II (Sivanandam et al. 2009).

## 6.2 BCG contribution to surface density

A surface brightness threshold is sometimes applied to images to separate ICL from the light of BCGs and/or other cluster galaxies (typically in the range 25–27 mag arcsec $^{-2}$ ; Zibetti et al. 2005; Rudick et al. 2011). Our models can be used to determine how ‘efficient’ such cuts are, in terms of the fraction of the total accreted

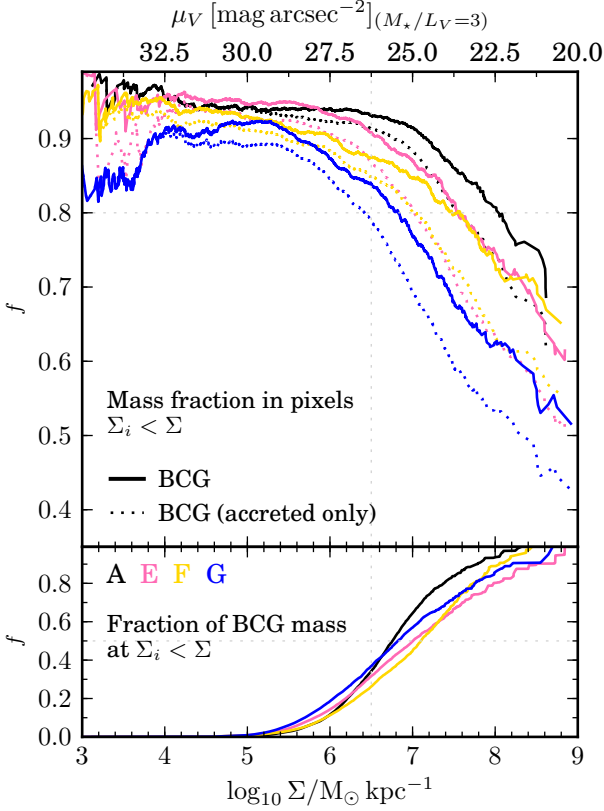


**Figure 16.** Top panel: cumulative distribution of BCG stellar mass (as a fraction of total stellar mass) in  $1 \text{ kpc}^2$  pixels below a given stellar mass surface density  $\Sigma$ . Upper axis converts  $\Sigma$  to  $V$ -band surface brightness assuming a mass-to-light ratio of 3. Dotted lines exclude in situ stars. Bottom panel: fraction of total BCG stellar mass in  $1 \text{ kpc}^2$  pixels with surface density less than  $\Sigma$ . The  $\Sigma = 10^{6.5} \text{ M}_\odot \text{ kpc}^{-2}$  contour is a good empirical threshold for the diffuse BCG envelope: selecting all pixels below this density maximises the fraction of light per pixel due to the BCG ( $\gtrsim 80$  per cent) while also recovering  $\sim 30$  per cent of its total stellar mass.

BCG mass they recover, and how ‘pure’ they are, in terms of the fraction of recovered light per pixel that is really due to the BCG rather than faint cluster galaxies.

The top panel of Fig. 15 shows a simple ‘SDSS like’ mock observation: a  $1 \text{ Mpc}^2$  image of the centre of cluster Ph-E with  $1 \text{ kpc}^2$  pixels. The lower panel shows only those stars associated with the BCG as we define it. Fig. 16 shows the cumulative fraction of stellar mass in all pixels below a given surface brightness that is associated with the BCG. The remainder is associated with other cluster galaxies. The bottom panel shows the fraction of the BCG’s total mass in pixels below a given surface density.

For an image such as Fig. 15, 90 to 95 per cent of the stellar mass in pixels with  $\Sigma < 10^5 \text{ M}_\odot \text{ kpc}^{-2}$  belongs to the BCG, but this accounts for  $\lesssim 1$  per cent of its total stellar mass. Over  $\gtrsim 80$  per cent of the mass in pixels with a stellar mass surface density  $\Sigma < 10^{6.5} \text{ M}_\odot \text{ kpc}^{-2}$  is associated with the BCG. Almost all of this is accreted (compare dotted and solid lines). The in situ contribution to the BCG increases at higher  $\Sigma$ , as does the contribution from other cluster galaxies.

A threshold of  $\Sigma \lesssim 10^{6.5} \text{ M}_\odot \text{ kpc}^{-2}$  ( $\mu_V \gtrsim 26.5$ ) is a reasonable compromise, selecting  $\sim 30$  per cent of the BCG mass at  $\gtrsim 80$  per cent purity. Hence our simulations predict that approximately 20 per cent of the luminosity in pixels fainter than this

threshold is associated to surviving galaxies. This prediction can be compared to measurements of the luminosity contributed by unresolved galaxies and the low surface brightness regions of resolved galaxies in real images. If stars associated to galaxies with sub-resolution haloes are counted towards the BCG mass, the purity a  $\Sigma \lesssim 10^{6.5} \text{ M}_\odot \text{ kpc}^{-2}$  becomes 50 to 70 per cent (see appendix A). This suggests that the distribution of pixel surface brightness in deep photometric observations might be a useful way to constrain theoretical models of galaxy disruption and stellar stripping.

## 7 CONCLUSIONS

We have applied a combination of semi-analytic and  $N$ -body modelling to the problem of diffuse light in massive galaxy clusters, following the particle tagging methodology introduced by Cooper et al. (2010) and used by C13 to study less massive groups and clusters. Our approach results in detailed predictions for the phase space distribution of stars in clusters based on a standard theory of cluster galaxy formation in  $\Lambda$ CDM (Kauffmann et al. 1993; Springel et al. 2001; De Lucia et al. 2004) constrained by the observed  $z = 0$  galaxy stellar mass function (Guo et al. 2011). Our  $N$ -body model has substantially higher resolution than most hydrodynamical simulations of very massive clusters.

Our main results concern the stellar mass surface density profiles of BCGs in  $M_{200} \sim 10^{15} \text{ M}_\odot$  clusters and the fraction of stellar mass in these clusters that is bound to their central potential. They are as follows:

(i) *BCG mass and morphology are dominated by stars accreted from other galaxies, even within their half mass radius.* The suppression of in situ formation in massive haloes (arising in our model from the combination of AGN feedback and long radiative cooling timescales) tends to enhance the importance of accretion (e.g. Puchwein et al. 2010). In situ star formation contributes of the order of 10 per cent of the total BCG mass and does not significantly affect the surface brightness profile beyond 10 kpc.

(ii) *In context of the  $\Lambda$ CDM model, ‘ICL’ is most naturally considered as a continuation of BCG structure to low surface brightness, rather than a separate galactic component with a distinct formation mechanism.* We find no evidence to motivate the ‘subtraction’ of an ICL component in the photometric analysis of BCGs. Light in low surface brightness regions should be consistently accounted for in measurements of individual BCGs and their population statistics, for example in distributions of BCG size and mass.

(iii) *Galaxy clusters are rich in dynamical substructure.* In low surface brightness regions ( $30 \lesssim \mu \lesssim 25 \text{ mag arcsec}^{-2}$ ) our nine clusters show many faint stellar overdensities with stream and shell morphologies. These result from episodic tidal stripping of galaxies  $\lesssim 10$  per cent of the BCG mass over several gigayears, driving substantial evolution of the BCG SB profile at  $R \gtrsim 100 \text{ kpc}$  between  $z = 1$  and  $z = 0.25$ .

(iv) *Many cluster galaxies are still being actively stripped at  $z = 0$ .* Approximately 20 per cent of stars accreted by the BCG have been stripped from surviving dark matter subhaloes above our resolution limit. Even so, coherent streams with  $\mu_V \sim 25 \text{ mag arcsec}^{-2}$  are rare, consistent with counts in very nearby clusters. Fainter streams are more common but have low surface density contrast with other diffuse debris.

(v) *BCG surface brightness profiles have a characteristic double Sérsic form.* This emerges from the superposition of many separate debris components from different progenitors. Taken in rank



order of mass, at least 40 progenitors are required to account for 90 per cent of the BCG mass.

(vi) *The profile of each progenitor debris component can be classified (loosely) as either ‘relaxed’ or ‘unrelaxed’.* ‘Relaxed’ components are centrally concentrated and roughly symmetric around the BCG. They are associated with early accretion events and/or mergers with low mass ratios leading to violent relaxation (White 1978; Naab et al. 2006; Oser et al. 2010; Hilz et al. 2012). ‘Unrelaxed’ components are more diffuse and include the distended envelopes of other bright cluster galaxies.

(vii) *In circular apertures centred on the BCG, ‘unrelaxed’ debris components are characterised by profiles with large effective radius and low Sersic index ( $n \lesssim 2$ ).* When the total mass in these components is significant (as for example in recently merged clusters with several BCG candidates) the BCG surface brightness profile breaks to a shallower slope at large radii (relative to regions with  $\mu \sim 24 \text{ mag arcsec}^{-2}$ , which typically have  $n \gtrsim 4$ ). The outer component of a double Sersic fit is a good estimate of the net ‘unrelaxed’ contribution in most cases.

(viii) *Our results support observational evidence for diffuse  $n \sim 1$  components in BCG profiles* (Seigar et al. 2007; Donzelli et al. 2011). Qualitatively, such outer exponential components are similar to the ‘cD envelope’ phenomenon. In our simulations, this phenomenon does not occur in all clusters of similar  $M_{200}$ . In some cases, it originates from the tidal debris of another massive cluster member, while in others it originates from multiple accretion events. A much larger suite of simulations is necessary for a statistical study of relationships between the assembly history of BCGs and the parameters of their surface brightness profiles.

(ix) *The BCG stellar mass fraction in our model has a strong  $M_{200}$  dependence that extends up to the most massive clusters ( $M_{200} \sim 10^{15} M_{\odot}$ ).* This global trend is very similar to that seen in observational data. The largest disagreement between our model and the data is of the order of  $\sim 20$  per cent and occurs in the halo mass range  $10^{13} < M_{200} < 10^{14} M_{\odot}$ . Radial trends in the BCG mass fraction also agree well.

(x) *For an SDSS-like observation, ( $z \approx 0.15$ ,  $1 \text{ kpc pixels}$ ), a surface brightness threshold of  $\Sigma \lesssim 6.5 M_{\odot} \text{ kpc}^{-2}$  ( $\mu_V \sim 26 \text{ mag arcsec}^{-2}$ ) is a reasonable first order cut to isolate the accreted component of the BCG.* In simulated images, this cut recovers 30 per cent of the BCG mass, almost all of which is accreted, and requires only a  $\sim 20$  per cent correction for light from other cluster members.

In summary, we find generally good agreement between our model and the low-redshift galaxy cluster data of Gonzalez et al. (2007) and Donzelli et al. (2011). This implies that the G11 semi-analytic model assigns plausible stellar masses to at least the most significant progenitors of present day BCGs (see also Laporte et al. 2013). The number, mass ratio, timing and orbits of merger events, which emerge naturally from our  $\Lambda$ CDM initial conditions, must also be consistent with the constraints inferred from idealized merger simulations (e.g. Hilz et al. 2013).

On the other hand, we find disagreement between our results and the observational data of Bildfell et al. (2008) and a 0.2 dex overestimate of  $R_{50}$  with respect to an extrapolation of the SerExp relation of Bernardi et al. (2012). At face value, these discrepancies suggest that the G11 model may overestimate the luminosity of the most massive BCG progenitors in haloes with  $M_{200} \sim 10^{15} M_{\odot}$ . Further work is required to understand how uncertainties in the semi-analytic model affect this result. In particular, the G11 model is known to overpredict the number of galaxies less massive than

the Milky Way at  $z \gtrsim 1$  (G11; Henriques et al. 2013). Such galaxies may contribute to the outer parts of the BCG profile at  $z = 0$ , either directly or through their contribution to the envelopes of major BCG progenitors.

In common with Contini et al. (2014), we find that conclusions regarding diffuse light in simulations are disproportionately sensitive to the fate of relatively few massive progenitors (those with  $\sim 1$  to 10 per cent of the BCG mass<sup>10</sup>). Robust quantitative conclusions about the fraction and profile of intracluster light require high numerical resolution and well understood numerical convergence, in terms of both satellite galaxy orbits and star formation histories. Even at the resolution of Phoenix, the finite resolution of dark matter subhalos introduces uncertainties of up to  $\sim 20$  per cent. Modelling the formation and dynamics of galaxies at high enough resolution across the wide range of scales relevant to galaxy clusters is a challenge to all models, whether  $N$ -body, hydrodynamic or semi-analytic. We conclude from the results above that our hybrid particle tagging approach is successful enough to merit further comparison with data on the low surface brightness regions of galaxy clusters.

## ACKNOWLEDGMENTS

We thank Anthony Gonzalez and Stefano Zibetti for providing their observational data. This work was carried out as part of the MPA Garching – NAOC Partner Group of the Max-Planck Society. Phoenix is a project of the Virgo Consortium. The simulations used in this work were carried out on the Lenovo Deepcomp7000 supercomputer at the Super Computing Center of the Chinese Academy of Sciences, Beijing, and on the Cosmology Machine at the Institute for Computational Cosmology, Durham. This work used the DiRAC Data Centric system at Durham University, operated by the Institute for Computational Cosmology on behalf of the STFC DiRAC HPC Facility ([www.dirac.ac.uk](http://www.dirac.ac.uk)). This equipment was funded by BIS National E-infrastructure capital grant ST/K00042X/1, STFC capital grant ST/H008519/1, and STFC DiRAC Operations grant ST/K003267/1 and Durham University. DiRAC is part of the National E-Infrastructure. APC acknowledges the support of a Chinese Academy of Sciences International Research Fellowship and NSFC grant no. 11350110323. CSF acknowledges support from an ERC Advanced Investigator grant, COSMIWAY. LG acknowledges support from an NSFC grant (No. 11133003), the MPG partner Group family, and an STFC Advanced Fellowship, as well as the hospitality of the Institute for Computational Cosmology at Durham University. QG acknowledges the support of NSFC grants (Nos. 11143005, 11133003) and an NAOC grant (No. Y434011V01). LG and QG are supported by the Strategic Priority Research Program “The Emergence of Cosmological Structure” of the Chinese Academy of Sciences (No. XDB09000000). VS acknowledges support by the European Research Council under ERC-StG grant EXAGAL-308037. SW was supported in part by ERC Advanced Grant 246797 “Galformod”.

<sup>10</sup> This contrasts with cluster galaxy luminosity and correlation functions, which are sensitive to a much larger number of less massive galaxies (e.g. Kim et al. 2009; Kang 2014; Guo & White 2014).

## REFERENCES

- Abadi M. G., Navarro J. F., Fardal M., Babul A., Steinmetz M., 2010, *MNRAS*, 407, 435
- Adami C., Slezak E., Durret F., Conselice C. J., Cuillandre J. C., Gallagher J. S., Mazure A., Pelló R., Picat J. P., Ulmer M. P., 2005, *A&A*, 429, 39
- Applegate D. E., von der Linden A., Kelly P. L., Allen M. T., Allen S. W., Burchat P. R., Burke D. L., Ebeling H., Mantz A., Morris R. G., 2014, *MNRAS*, 439, 48
- Aragon-Salamanca A., Baugh C. M., Kauffmann G., 1998, *MNRAS*, 297, 427
- Balogh M. L., McCarthy I. G., Bower R. G., Eke V. R., 2008, *MNRAS*, 385, 1003
- Bernardi M., Meert A., Sheth R. K., Vikram V., Huertas-Company M., Mei S., Shankar F., 2013, *MNRAS*, 436, 697
- Bernardi M., Meert A., Vikram V., Huertas-Company M., Mei S., Shankar F., Sheth R. K., 2012, *ArXiv e-prints*, astro-ph/1211.6122
- Bernstein G. M., Nichol R. C., Tyson J. A., Ulmer M. P., Wittman D., 1995, *AJ*, 110, 1507
- Bildfell C., Hoekstra H., Babul A., Mahdavi A., 2008, *MNRAS*, 389, 1637
- Bower R. G., McCarthy I. G., Benson A. J., 2008, *MNRAS*, 390, 1399
- Boylan-Kolchin M., Springel V., White S. D. M., Jenkins A., 2010, *MNRAS*, 406, 896
- Budzynski J. M., Koposov S. E., McCarthy I. G., Belokurov V., 2014, *MNRAS*, 437, 1362
- Calcáneo-Roldán C., Moore B., Bland-Hawthorn J., Malin D., Sadler E. M., 2000, *MNRAS*, 314, 324
- Cole S., Lacey C. G., Baugh C. M., Frenk C. S., 2000, *MNRAS*, 319, 168
- Conroy C., Wechsler R. H., Kravtsov A. V., 2007, *ApJ*, 668, 826
- Conselice C. J., Gallagher III J. S., 1999, *AJ*, 117, 75
- Contini E., De Lucia G., Villalobos Á., Borgani S., 2014, *MNRAS*, 437, 3787
- Cooper A. P., Cole S., Frenk C. S., White S. D. M., Helly J., Benson A. J., De Lucia G., Helmi A., Jenkins A., Navarro J. F., Springel V., Wang J., 2010, *MNRAS*, 406, 744
- Cooper A. P., D'Souza R., Kauffmann G., Wang J., Boylan-Kolchin M., Guo Q., Frenk C. S., White S. D. M., 2013, *MNRAS*, 434, 3348
- Cooper A. P., Martínez-Delgado D., Helly J., Frenk C., Cole S., Crawford K., Zibetti S., Carballo-Bello J. A., GaBany R. J., 2011, *ApJ*, 743, L21
- De Lucia G., Blaizot J., 2007, *MNRAS*, 375, 2
- De Lucia G., Kauffmann G., White S. D. M., 2004, *MNRAS*, 349, 1101
- Diemand J., Madau P., Moore B., 2005, *MNRAS*, 364, 367
- Dolag K., Murante G., Borgani S., 2010, *MNRAS*, 405, 1544
- Donzelli C. J., Muriel H., Madrid J. P., 2011, *ApJS*, 195, 15
- D'Souza R., Kauffmann G., Wang J., Vegetti S., 2014, *ArXiv e-prints*, astro-ph/1404.2123
- Dubinski J., 1998, *ApJ*, 502, 141
- Dutton A. A., Treu T., 2014, *MNRAS*, 438, 3594
- Dutton A. A., van den Bosch F. C., Dekel A., Courteau S., 2007, *ApJ*, 654, 27
- El-Zant A., Shlosman I., Hoffman Y., 2001, *ApJ*, 560, 636
- Feldmeier J. J., Mihos J. C., Morrison H. L., Harding P., Kaib N., Dubinski J., 2004, *ApJ*, 609, 617
- Frenk C. S., White S. D. M., Efstathiou G., Davis M., 1985, *Nature*, 317, 595
- Gal-Yam A., Maoz D., Guhathakurta P., Filippenko A. V., 2003, *AJ*, 125, 1087
- Gallagher III J. S., Ostriker J. P., 1972, *AJ*, 77, 288
- Gao L., Loeb A., Peebles P. J. E., White S. D. M., Jenkins A., 2004, *ApJ*, 614, 17
- Gao L., Navarro J. F., Frenk C. S., Jenkins A., Springel V., White S. D. M., 2012, *MNRAS*, 425, 2169
- Gnedin O. Y., Kravtsov A. V., Klypin A. A., Nagai D., 2004, *ApJ*, 616, 16
- Gonzalez A. H., Zabludoff A. I., Zaritsky D., 2005, *ApJ*, 618, 195
- Gonzalez A. H., Zaritsky D., Zabludoff A. I., 2007, *ApJ*, 666, 147
- Graham A., Lauer T. R., Colless M., Postman M., 1996, *ApJ*, 465, 534
- Graham A. W., Driver S. P., 2005, *PASA*, 22, 118
- Gregg M. D., West M. J., 1998, *Nature*, 396, 549
- Guo Q., White S., 2014, *MNRAS*, 437, 3228
- Guo Q., White S., Angulo R. E., Henriques B., Lemson G., Boylan-Kolchin M., Thomas P., Short C., 2013, *MNRAS*, 428, 1351
- Guo Q., White S., Boylan-Kolchin M., De Lucia G., Kauffmann G., Lemson G., Li C., Springel V., Weinmann S., 2011, *MNRAS*, 413, 101
- Guo Q., White S. D. M., 2008, *MNRAS*, 384, 2
- Guo Y., McIntosh D. H., Mo H. J., Katz N., van den Bosch F. C., Weinberg M., Weinmann S. M., Pasquali A., Yang X., 2009, *MNRAS*, 398, 1129
- Hausman M. A., Ostriker J. P., 1978, *ApJ*, 224, 320
- Helmi A., 2008, *A&A Rev.*, 15, 145
- Henriques B. M. B., Thomas P. A., 2010, *MNRAS*, 403, 768
- Henriques B. M. B., White S. D. M., Thomas P. A., Angulo R. E., Guo Q., Lemson G., Springel V., 2013, *MNRAS*, 431, 3373
- Hilz M., Naab T., Ostriker J. P., 2013, *MNRAS*, 429, 2924
- Hilz M., Naab T., Ostriker J. P., Thomas J., Burkert A., Jesseit R., 2012, *MNRAS*, 425, 3119
- Janowiecki S., Mihos J. C., Harding P., Feldmeier J. J., Rudick C., Morrison H., 2010, *ApJ*, 715, 972
- Kang X., 2014, *MNRAS*, 437, 3385
- Kauffmann G., White S. D. M., Guiderdoni B., 1993, *MNRAS*, 264, 201
- Kim H.-S., Baugh C. M., Cole S., Frenk C. S., Benson A. J., 2009, *MNRAS*, 400, 1527
- Krick J. E., Bernstein R. A., 2007, *AJ*, 134, 466
- Krick J. E., Bernstein R. A., Pimbblet K. A., 2006, *AJ*, 131, 168
- Laporte C. F. P., White S. D. M., Naab T., Gao L., 2013, *MNRAS*, 435, 901
- Laporte C. F. P., White S. D. M., Naab T., Ruzsowski M., Springel V., 2012, *MNRAS*, 424, 747
- Li Y.-S., White S. D. M., 2008, *MNRAS*, 384, 1459
- Lin Y.-T., Mohr J. J., 2004, *ApJ*, 617, 879
- Liu F. S., Xia X. Y., Mao S., Wu H., Deng Z. G., 2008, *MNRAS*, 385, 23
- Lugger P. M., 1984, *ApJ*, 286, 106
- Mackie G., Visvanathan N., Carter D., 1990, *ApJS*, 73, 637
- Martínez-Delgado D., Gabany R. J., Crawford K., Zibetti S., Majewski S. R., Rix H.-W., Fliri J., Carballo-Bello J. A., Bardalez-Gagliuffi D. C., Peñarrubia J., Chonis T. S., Madore B., Trujillo I., Schirmer M., McDavid D. A., 2010, *AJ*, 140, 962
- Martizzi D., Teyssier R., Moore B., 2012, *MNRAS*, 420, 2859
- Matthews T. A., Morgan W. W., Schmidt M., 1964, *ApJ*, 140, 35
- McConnachie A. W., 2012, *AJ*, 144, 4
- McGee S. L., Balogh M. L., 2010, *MNRAS*, 403, L79

- Melnick J., Hoessel J., White S. D. M., 1977, *MNRAS*, 180, 207
- Merritt D., 1984, *ApJ*, 276, 26
- Mihos J. C., Harding P., Feldmeier J., Morrison H., 2005, *ApJ*, 631, L41
- Monaco P., Murante G., Borgani S., Fontanot F., 2006, *ApJ*, 652, L89
- Moore B., Katz N., Lake G., Dressler A., Oemler A., 1996, *Nature*, 379, 613
- Murante G., Arnaboldi M., Gerhard O., Borgani S., Cheng L. M., Diaferio A., Dolag K., Moscardini L., Tormen G., Tornatore L., Tozzi P., 2004, *ApJ*, 607, L83
- Murante G., Giovali M., Gerhard O., Arnaboldi M., Borgani S., Dolag K., 2007, *MNRAS*, 377, 2
- Naab T., Johansson P. H., Ostriker J. P., 2009, *ApJ*, 699, L178
- Naab T., Khochfar S., Burkert A., 2006, *ApJ*, 636, L81
- Napolitano N. R., Pannella M., Arnaboldi M., Gerhard O., Aguerri J. A. L., Freeman K. C., Capaccioli M., Ghigna S., Governato F., Quinn T., Stadel J., 2003, *ApJ*, 594, 172
- Navarro J. F., Eke V. R., Frenk C. S., 1996, *MNRAS*, 283, L72
- Newman A. B., Treu T., Ellis R. S., Sand D. J., 2013a, *ApJ*, 765, 25
- Newman A. B., Treu T., Ellis R. S., Sand D. J., Nipoti C., Richard J., Jullo E., 2013b, *ApJ*, 765, 24
- Oemler Jr. A., 1976, *ApJ*, 209, 693
- Oser L., Ostriker J. P., Naab T., Johansson P. H., Burkert A., 2010, *ApJ*, 725, 2312
- Ostriker J. P., Tremaine S. D., 1975, *ApJ*, 202, L113
- Patel P., Maddox S., Pearce F. R., Aragón-Salamanca A., Conway E., 2006, *MNRAS*, 370, 851
- Piffaretti R., Arnaud M., Pratt G. W., Pointecouteau E., Melin J.-B., 2011, *A&A*, 534, A109
- Pontzen A., Governato F., 2012, *MNRAS*, 421, 3464
- Puchwein E., Springel V., Sijacki D., Dolag K., 2010, *MNRAS*, 406, 936
- Purcell C. W., Bullock J. S., Zentner A. R., 2007, *ApJ*, 666, 20
- Remus R.-S., Burkert A., Dolag K., Johansson P. H., Naab T., Oser L., Thomas J., 2013, *ApJ*, 766, 71
- Richstone D. O., 1975, *ApJ*, 200, 535
- Rozo E., Bartlett J. G., Evrard A. E., Rykoff E. S., 2014, *MNRAS*, 438, 78
- Rozo E., Rykoff E. S., Evrard A., Becker M., McKay T., Wechsler R. H., Koester B. P., Hao J., Hansen S., Sheldon E., Johnston D., Annis J., Frieman J., 2009, *ApJ*, 699, 768
- Rudick C. S., Mihos J. C., Harding P., Feldmeier J. J., Janowiecki S., Morrison H. L., 2010, *ApJ*, 720, 569
- Rudick C. S., Mihos J. C., McBride C., 2006, *ApJ*, 648, 936
- Rudick C. S., Mihos J. C., McBride C. K., 2011, *ApJ*, 732, 48
- Ruszkowski M., Springel V., 2009, *ApJ*, 696, 1094
- Sand D. J., Graham M. L., Bildfell C., Foley R. J., Pritchett C., Zaritsky D., Hoekstra H., Just D. W., Herbert-Fort S., Sivanandam S., 2011, *ApJ*, 729, 142
- Scannapieco C., Wadepuhl M., Parry O. H., Navarro J. F., Jenkins A., Springel V., Teyssier R., Carlson E., Couchman H. M. P., Crain R. A., Dalla Vecchia C., Frenk C. S., Kobayashi C., Monaco P., Murante G., Okamoto T., Quinn T., Schaye J., Stinson G. S., Theuns T., Wadsley J., White S. D. M., Woods R., 2012, *MNRAS*, 423, 1726
- Schombert J. M., 1986, *ApJS*, 60, 603
- , 1988, *ApJ*, 328, 475
- , 2013, *PASA*, 30, 34
- Seigar M. S., Graham A. W., Jerjen H., 2007, *MNRAS*, 378, 1575
- Sivanandam S., Zabludoff A. I., Zaritsky D., Gonzalez A. H., Kelson D. D., 2009, *ApJ*, 691, 1787
- Sommer-Larsen J., Romeo A. D., Portinari L., 2005, *MNRAS*, 357, 478
- Springel V., White S. D. M., Tormen G., Kauffmann G., 2001, *MNRAS*, 328, 726
- Thuan T. X., Kormendy J., 1977, *PASP*, 89, 466
- Trentham N., Mobasher B., 1998, *MNRAS*, 293, 53
- Uson J. M., Boughn S. P., Kuhn J. R., 1991, *ApJ*, 369, 46
- van Daalen M. P., Schaye J., Booth C. M., Dalla Vecchia C., 2011, *MNRAS*, 415, 3649
- White S. D. M., 1976, *MNRAS*, 174, 19
- , 1978, *MNRAS*, 184, 185
- , 1980, *MNRAS*, 191, 1P
- White S. D. M., Rees M. J., 1978, *MNRAS*, 183, 341
- Widrow L. M., 2000, *ApJS*, 131, 39
- Willman B., Governato F., Wadsley J., Quinn T., 2004, *MNRAS*, 355, 159
- Zibetti S., White S. D. M., Schneider D. P., Brinkmann J., 2005, *MNRAS*, 358, 949
- Zwicky F., 1951, *PASP*, 63, 61

This paper has been typeset from a  $\text{\LaTeX}$  file prepared by the author.

## APPENDIX A: NUMERICAL RESOLUTION

### A1 Convergence

Fig. A1 compares the BCG surface density profile in Ph-A at ‘level 2’ resolution (black solid line), used throughout this paper, with its equivalent at the lower ‘level 4’ resolution (a factor of 27 increase in particle mass; grey solid line). The profile appears well converged overall, although residuals can be up to  $\sim 50$  per cent, with the largest deviations at  $R < 10$  kpc (due to the increased softening length,  $\sim 1$  kpc at level 4) and  $R \gtrsim 200$  kpc. These differences may be due to stochastic changes in halo orbits and the timing of accretion events, as well as more rapid tidal stripping at lower resolution.

### A2 Tagging fraction

We use the constant tagging fraction approximation of Cooper et al. (2010) and C13, with  $f_{\text{mb}} = 1$  per cent. The red solid line in Fig. A1 compares the result for Ph-A with  $f_{\text{mb}} = 5$  per cent. The effects are similar to those with lower numerical resolution in the outer part of the halo, where higher  $f_{\text{mb}}$  results in less tightly bound galactic envelopes that are more easily stripped in the cluster. The behaviour at  $R < 10$  kpc is the result of a larger in situ scale length as described in C13 (in situ stars dominate this part of the profile in Ph-A).

### A3 Sub-resolution haloes

In the G11 semi-analytic model, galaxies can survive even when their associated dark matter halo is lost from the underlying  $N$ -body simulation after being stripped below the 20-particle resolution limit of SUBFIND. The timescale for merging or disrupting these galaxies is determined by simple semi-analytic recipes that approximate the orbital evolution of each satellite. This mechanism

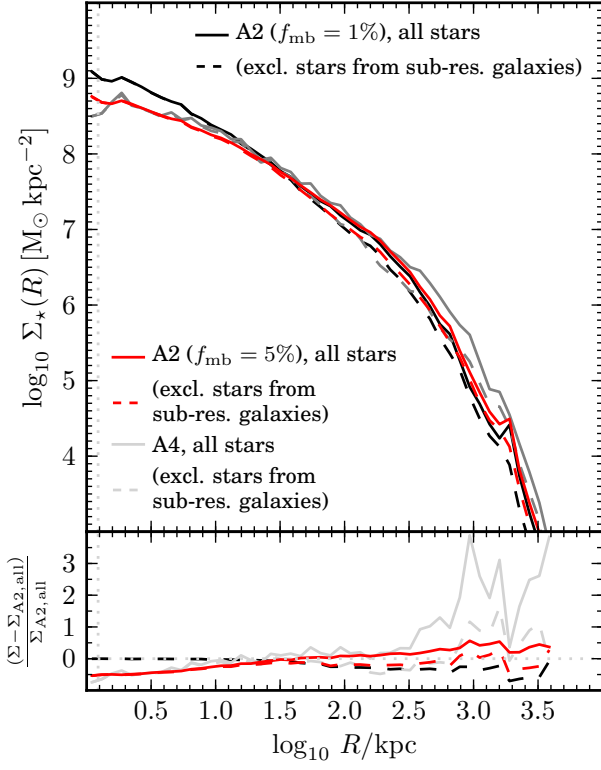


**Figure A1.** Top: the stellar surface density profile of the BCG in Ph-A (black) including stars associated sub-resolution haloes (our default model; solid) and excluding all such stars (dashed). Equivalent profiles are shown for a larger value of our parameter controlling how deeply new stars are embedded in their host dark matter potential,  $f_{\text{mb}} = 5$  per cent (red), and for lower resolution (grey). Bottom: residuals around our default model (black dashed line).

makes galaxy survival in the semi-analytic model much less sensitive to the resolution of the underlying N-body simulation (Guo & White 2014). Galaxies associated with these sub-resolution haloes are referred to in other work on the G11 model as ‘orphans’ or ‘type 2’ galaxies. Comparisons with observed luminosity and correlation functions constrain the number of galaxies that these recipes need to ‘keep alive’ to  $z = 0$  (see figures 14 and 19 of G11).

In our particle tagging scheme, all galaxies are, by definition, only as well resolved as their dark matter haloes. As described in the main text, we therefore need to decide whether to count stars associated with surviving sub-resolution semi-analytic galaxies as part of the BCG (following the N-body model) or not (following the semi-analytic model). The ‘best’ (numerically converged) answer will lie somewhere between the two: the semi-analytic model does not allow for the tidal stripping of stars from sub-resolution haloes, while N-body particle tagging overestimates it, because some stars may be bound to the unresolved core and the binding energy of the excess baryons is ignored.

Our fiducial choice is to follow the N-body simulation and treat all stars from sub-resolution semi-analytic galaxies as part of the BCG. Our principle argument in favour of this approach is given in the main text: the halo resolution limit of Phoenix corresponds to  $\sim 0.02$  per cent of  $M_{200}$  for a Milky Way-mass halo. This extreme mass loss makes it likely that a large fraction of the stars in such haloes will have been stripped by the time the dark matter is reduced to

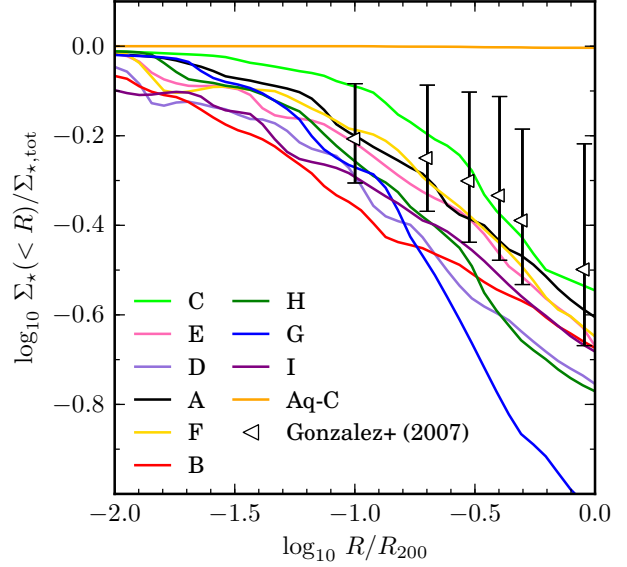


**Figure A2.** As Fig. 14 but excluding all stars associated with semi-analytic dark matter haloes below the resolution of the N-body simulation at  $z = 0$  from the definition of the BCG. The curves are systematically lower by  $\sim 0.1$  dex and the variation between haloes is greater.

this limit, regardless of whether the unresolved core remains bound or not.

This assumption will be less accurate for less massive haloes. Between 90 and 60 per cent (median  $\sim 84$  per cent) of the total stellar mass contributed to the accreted component of the BCG by galaxies associated with sub-resolution haloes comes from  $\lesssim 10$  galaxies more massive than  $M_* = 10^{10} M_\odot$ , (i.e. halos of  $M_{200} \gtrsim 10^{12} M_\odot$ , for which considerable stellar stripping before the time of halo disruption is likely). Less massive haloes, e.g. those of  $M_{200} \lesssim 10^{10} M_\odot$ , may retain a significant fraction of their stars when they cross the resolution limit. However, these correspond to galaxies of  $M_* \lesssim 10^8 M_\odot$ , which account for only 1 to 4 per cent of the stellar mass accreted from sub-resolution haloes.

Treating galaxies with sub-resolution haloes as disrupted alters previously established results from the G11 model to an extent that depends on N-body resolution. At the relatively high resolution of Millennium II, only a small fraction of massive galaxies in clusters have sub-resolution haloes and they do not dominate the agreement between the model and the overall galaxy population in the field<sup>11</sup>. G11 show that 14 per cent of  $\sim 10^{14} M_\odot$  cluster member galaxies more massive than the Milky Way belong to sub-resolution haloes in Millennium II, mostly projected within  $R < 200$  kpc. In further support of our fiducial choice, figures 14 and 19 of G11 suggest that their model produces more of these galaxies than observational data imply. Reducing the number predicted in Millennium II by  $\sim 20$  per cent would improve agreement with SDSS results on the radial distribution of galaxies in clusters and the field galaxy two-point correlation function (Marcel van Daalen, private communication).

<sup>11</sup> It is likely that a slightly larger number of bound cores will survive in Phoenix compared to Millennium II, because Phoenix has a similar particle mass and an even smaller force softening length.



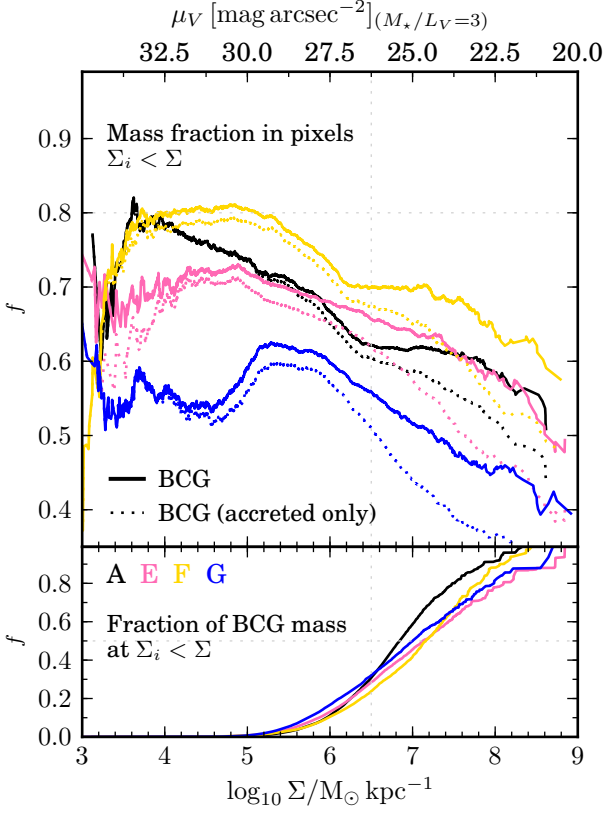


**Figure A3.** As Fig. 16, but excluding all stars associated with semi-analytic dark matter haloes below the resolution of the  $N$ -body simulation at  $z = 0$  from the definition of the BCG. The relatively large changes seen in the upper panel are caused by the assignment of stars in very low surface brightness pixels to cluster galaxies rather than the BCG. Measurements of this distribution from deep photometry could therefore constrain models of galaxy disruption in clusters.

Fig. A1 shows the effect of stars from sub-resolution haloes on the overall BCG density profile of Ph-A. The solid black line shows the profile we adopt in the main text, which includes stars associated with surviving sub-resolution haloes. The dashed black line shows the same profile with those stars excluded. The difference appears small in these logarithmic plots, and mainly affects radii  $R \gtrsim 100$  kpc. Nevertheless (as shown in table 1), excluding stars from sub-resolution haloes reduces the total stellar mass of the BCG by  $\sim 28$  per cent. This fraction is similar for the other haloes. Fig. 14 shows that this strongly affects the stellar mass fraction attributed to the BCG beyond  $0.1 R_{200}$ , and this in turn alters the global 'BCG/total' mass ratio shown in Fig. 12 by  $\sim 0.2$  dex. As expected, Fig. A1 also shows that including stars from sub-resolution haloes in the BCG definition increases differences in the BCG density profile due to numerical resolution and the choice of  $f_{\text{mb}}$ .

Figs. A2 and A3 repeat Figs. 14 and 16 from the main text. Of all our results, these figures are most sensitive to the treatment of stars associated with sub-resolution haloes. The discrepancy between Fig. A2 and Fig. 14 increases steadily to larger radii, reflecting the increasing fractional contribution of the uncertain stellar component further from the BCG seen in Fig. A1. The small changes in the lower panel of Fig. A3, relative to that of Fig. 16, confirm that this uncertainty mainly affects low surface brightness

regions, which do not contribute a large fraction of the total stellar mass of the BCG.